Three-Dimensional Variational Multi-Doppler Wind Retrieval over Complex Terrain

TING-YU CHA[a] AND MICHAEL M. BELL[b]

[a] *National Center for Atmospheric Research, Boulder, Colorado*
[b] *Department of Atmospheric Science, Colorado State University, Fort Collins, Colorado*

(Manuscript received 7 February 2023, in final form 10 August 2023, accepted 24 August 2023)

ABSTRACT: The interaction of airflow with complex terrain has the potential to significantly amplify extreme precipitation events and modify the structure and intensity of precipitating cloud systems. However, understanding and forecasting such events is challenging, in part due to the scarcity of direct in situ measurements. Doppler radar can provide the capability to monitor extreme rainfall events over land, but our understanding of airflow modulated by orographic interactions remains limited. The SAMURAI software is a three-dimensional variational data assimilation (3DVAR) technique that uses the finite element approach to retrieve kinematic and thermodynamic fields. The analysis has high fidelity to observations when retrieving flows over a flat surface, but the capability of imposing topography as a boundary constraint is not previously implemented. Here, we implement the immersed boundary method (IBM) as pseudo-observations at their native coordinates in SAMURAI to represent the topographic forcing and surface impermeability. In this technique, neither data interpolation onto a Cartesian grid nor explicit physical constraint integration during the cost function minimization is needed. Furthermore, the physical constraints are treated as pseudo-observations, offering the flexibility to adjust the strength of the boundary condition. A series of observing simulation sensitivity experiments (OSSEs) using a full-physics model and radar emulator simulating rainfall from Typhoon Chanthu (2021) over Taiwan are conducted to evaluate the retrieval accuracy and parameter settings. The OSSE results show that the strength of the IBM constraints can impact the overall wind retrievals. Analysis from real radar observations further demonstrates that the improved retrieval technique can advance scientific analyses for the underlying dynamics of orographic precipitation using radar observations.

KEYWORDS: Tropical cyclones; Radars/Radar observations; Variational analysis; Cloud resolving models; Orographic effects

1. Introduction

The vertical transport of water vapor and air is crucial in the weather and climate system, yet vertical motion (w) remains one of the most challenging wind components to observe and predict accurately. In complex terrain, orographically induced airflow plays a significant role in modulating weather systems, impacting precipitation intensity and cloud structure. The interaction between clouds and topography involves various physical mechanisms that can lead to extreme rainfall and intense convective storms (Zipser et al. 2006; Chien and Kuo 2011; Houze 2012).

Doppler radar observations present an opportunity to understand the airflow associated with orographic interactions and the key ingredients that impact the intensity and duration of severe weather. Multiple Doppler radar observations can be used to reconstruct a full three-dimensional wind field (Ray et al. 1979), but the accuracy of w remains challenging, especially when the precipitating system is over a mountainous area (del Moral et al. 2020). Most state-of-the-art radar synthesis software currently incorporates the mass continuity equation to retrieve w throughout the atmospheric column. The mass continuity equation enforces the mass-weighted vertical flow to be physically consistent with the divergence of the mass-weighted horizontal flow. However, additional boundary conditions are necessary to impose physical constraints on airflow movement over terrain. An accurate representation of the boundary conditions is required to retrieve a reasonable three-dimensional wind field and to further study storm dynamics. In this study, we implement boundary conditions at the terrain height to represent the topographic forcing and surface impermeability in the three-dimensional variational data assimilation (3DVAR) multi-Doppler radar software for recovering the wind field over complex terrain.

Variational techniques have been widely used for multi-Doppler retrievals (Gamache et al. 1995; Gao et al. 1999, 2004; Potvin et al. 2012b; Bell et al. 2012; North et al. 2017). The 3DVAR approach solves for the optimal wind field by minimizing a cost function that incorporates various types of observations with specified uncertainties and the algorithm assumptions (e.g., mass continuity equation). Different sources of uncertainties include algorithm effects, instrument effects, and sampling effects. Algorithm effects include the interpolation and smoothing techniques used to map the radar polar grid to a common Cartesian coordinate system (Collis et al. 2010), hydrometeor fall speed estimates (Steiner 1991), and other algorithm assumptions (e.g., mass continuity integration; Matejka and Bartels 1998). Hildebrand et al. (1994) show that instrument effects can contribute to errors of up to 1 m s^{-1} in Doppler wind measurements due to radar processor design and measurement techniques. Sampling effects include data spacing and density, which are impacted by the geometry of dual or multiradar beams and beam blockage by terrain, as well as the temporal evolution of weather phenomena, and data collection time span (Hildebrand and Mueller 1985; Oue et al. 2019;

Corresponding author: Ting-Yu Cha, tycha@ucar.edu

DOI: 10.1175/JTECH-D-23-0019.1

Cha and Bell 2021). In Oue et al. (2019), a radar emulator was used to investigate the quality of vertical wind retrieval in relation to observational error sources. Their findings demonstrate that the choice of volume coverage pattern (VCP) elevation strategy and sampling time can significantly influence the accuracy of retrieved vertical velocity. Additionally, utilizing rapid-scan radars to reduce the data collection period can greatly enhance the quality of the results. Understanding and accounting for these uncertainties are crucial for accurate wind retrieval in the 3DVAR approach.

Most 3DVAR approaches have been developed for retrievals over flat surfaces, but retrievals over complex terrain require additional considerations of the topographic forcing and impermeability at the terrain height. Georgis et al. (2000) was one of the first studies that developed a variational approach to account for orographic effects in multi-Doppler radar analysis. In their approach, a first guess of the vertical velocity is derived through the integration of the mass continuity equation. The vertical wind is then iteratively solved until a converged solution is obtained. Chong and Cosma (2000) improved the variational multiple-Doppler synthesis and continuity adjustment technique (MUSCAT; Bousquet and Chong 1998) by implementing the capability to retrieve the wind field over complex terrain. Chong et al. (2000) further integrated the aforementioned approaches and presented an improved multiple-Doppler analysis method for real-time recovery of the wind field over mountainous regions, and a low-pass filter is used to partially recover the wind flow along the radar baseline. Employing a low-pass filter helps alleviate retrieval instabilities in areas with sparse data coverage and along the radar baseline.

Liou and Chang (2009) developed a variational multiple-Doppler radar three-dimensional wind synthesis method over flat terrain. The accuracy of vertical velocity retrieval was improved by incorporating the vertical vorticity equation and removing the assumption of prescribed vertical velocities at the data boundary. Building upon this work, Liou et al. (2012) further advanced the technique by introducing the immersed boundary method (IBM) with a ghost cell approach. This method allows for the recovery of the wind field above the terrain while considering the topographic forcing (Tseng and Ferziger 2003). The IBM approach provides realistic topographic forcing within a standard Cartesian grid, eliminating the need to convert to a terrain-following coordinate system. This capability allows for an accurate representation of the topographic effects without the requirement of transforming the coordinate system.

The Spline Analysis at Mesoscale Utilizing Radar and Aircraft Instrumentation (SAMURAI) analysis technique employs a finite element approach using a series of overlapping cubic B-spline basis functions. This approach offers several advantages over a conventional gridpoint representation (Bell et al. 2012; Foerster et al. 2014), including the following:

- The use of a finite element representation for functions allows for a scale-controlled analysis that can incorporate multiple spatial filters in the background error covariance and analytic spatial derivatives in observational space, eliminating the need of adding terms to the cost function to account for additional constraints. This feature enables the user to easily select the desired scales and constraints for an analysis.
- Traditional 3DVAR multi-Doppler approaches typically involve the interpolation of polar radar data to a Cartesian coordinate system, which can introduce artifacts in vertical velocities (Collis et al. 2010). In SAMURAI, the finite element method can handle irregular data distributions and complex immersed boundary geometries directly without interpolation to a Cartesian grid. Instead, the data can be used in the variational minimization in their native locations. This feature reduces one of the potential interpolation errors in the analysis.
- Spatial derivative constraints can be obtained from physical equations, such as the mass continuity equation and/or the momentum equations (Foerster et al. 2014). The finite element formulation allows for the specification of these derivative constraints as pseudo-observations at any point in their native coordinate. Physical constraints on the spatial gradients can be treated as pseudo-observations at any given point with specified pseudo-observational errors that are implicitly integrated during the cost function minimization rather than explicitly integrated.

The SAMURAI technique has demonstrated its ability to generate high-quality scientific results over flat surfaces, as evidenced by previous studies (Bell et al. 2012; Foerster et al. 2014; Martinez et al. 2019; Cha et al. 2020). However, when it comes to retrievals over complex terrain, additional assumptions regarding terrain boundaries need to be considered. The current study improves the SAMURAI technique by incorporating retrieval capabilities over complex terrain. We implement the IBM method as pseudo-observations which allows for the boundary conditions at any specified terrain height with adjustable pseudo-observational errors. The analytic nature of spatial derivatives eliminates the requirement for the ghost cell approach utilized in finite-difference methods. The outline of the paper is as follows: Section 2 describes the details and the formulation of the 3DVAR approach designed for use over complex terrain. Section 3 presents the dataset used and outlines the experimental setup to assess the accuracy of the immersed boundary solver. Observing system simulation experiments (OSSEs) are conducted using simulated data from Typhoon Chanthu (2021) which produced heavy rainfall over complex topography in northern Taiwan. Section 4 investigates the performance of the newly developed method through sensitivity tests on various experimental setups, including varying the strength of terrain forcing constraint at the boundary (section 4a), exploring the resolution and details of complex terrain slope (section 4b), assessing the contribution of vertical wind retrieval from mass continuity and terrain forcing (section 4c), and analyzing the impact of grid spacing and Gaussian recursive filter settings (section 4d). Section 5 demonstrates the applicability of the wind retrieval over complex terrain using real radar data from Typhoon Chanthu (2021). Section 6 provides a summary of the findings and discusses their implications.

2. Methodology

a. SAMURAI

SAMURAI uses a set of cubic B-spline basis functions that are continuous and differentiable up to the third-order derivative. Combining a set of spline functions allows for the formation of the shape of any function while still being differentiable. The use of spline basis functions in representing the atmospheric structure allows for the specification of pseudo-observations of spatial gradients.

The nodal spacing in SAMURAI determines the minimum feature size that can be resolved by the function. The finite element approach in SAMURAI provides flexibility in specifying nodal spacing and spatial gradients at any point and space, which allows for a more adaptable representation of the atmospheric structure. These pseudo-observations of spatial gradients are integrated during the cost function minimization, along with the observations and background. The cost function, formulated as an incremental form, incorporates weights based on observations, observation errors, background state estimates, and background state errors. The cost function is minimized at the most likely atmospheric state at the analysis time based on the input data and specified errors. SAMURAI initially employed a nonlinear conjugate gradient (NCG) method, which involved computationally intensive tasks such as evaluating the gradient and performing a line search in each iteration until convergence (Gao et al. 2004). Dennis et al. (2022) improved the optimization solver performance by implementing a truncated Newton (TN) solver, optimizing code, and porting SAMURAI to GPU environments, which results in a substantial reduction in the overall execution time. The combined improvement efforts have resulted in speed improvements exceeding 100 times compared to the original SAMURAI code. For more detailed information regarding these improvements, please refer to Dennis et al. (2022).

SAMURAI has three spatial filters to facilitate analysis smoothing and the propagation of information from observations throughout the domain, including the Fourier spectral filter, the spline cutoff, and the Gaussian recursive filter. The Fourier spectral filter is mainly used for removing high-wavenumber features directly in the spectral domain or restricting to a mean value along a particular axis (i.e., wavenumber zero only). The spline cutoff is implemented as a third derivative constraint on the cubic B-spline basis during the spline transform (Ooyama 2002). The Gaussian recursive filter operates as a Gaussian low-pass filter utilizing an efficient recursive operator (Purser et al. 2003). Smaller filter lengths retain more detail, albeit with a potential to capture noise, whereas larger filter lengths yield greater smoothing but may result in the loss of fine details. These filters can be used individually or in combination to produce different responses. Choosing an appropriate filter type and length based on the data distribution is crucial in obtaining the desired physical scales of interest in the analysis.

In this study, we utilized a combination of the spline cutoff filter with two nodes in the horizontal direction and the Gaussian recursive filter with four nodes in the horizontal and two nodes in the vertical direction. The sensitivity of the Gaussian recursive filter setting will be investigated in section 4, whereas the sensitivity of the Fourier filter and spline cutoff setting will not be addressed in this study.

b. The immersed boundary method

Urban and mountainous environments often feature steep slopes and complex geometries. The IBM method enables flows in such complex terrains to be simulated at their native spacing, without the need to conform to a specific coordinate system. This approach preserves the topography with high-order boundary representations, accurately capturing the intricate features of the terrain. This ensures that winds influenced by terrain forcing can be realistically resolved.

The IBM has been implemented into the Weather Research and Forecasting (WRF) Model (Lundquist et al. 2010) and an observational wind retrieval technique Wind Synthesis System using Doppler Measurements (WISSDOM; Liou et al. 2012). Previous studies have adopted a finite-difference approach, where the body force term is applied to ghost cells located within the terrain. This ghost cell method is able to handle rigid boundaries and produce a sharp representation of the fluid–solid interface. In SAMURAI, the ghost cell approach can be circumvented through two main implementations. First, the finite element approach is utilized, allowing the terrain boundary nodes to be positioned independently of specific computational nodes. This flexibility enables the boundary spatial derivatives to be computed at their original locations. Second, SAMURAI uses a set of overlapping cubic B-splines that are differentiable up to the third-order derivative (Fig. 1). This allows the boundary condition to be applied directly at the terrain height instead of using a traditional ghost cell.

Two boundary conditions are implemented into SAMURAI, following Liou et al.'s (2012) method:

$$\frac{\partial u}{\partial n} = 0 = \nabla \mathbf{u} \cdot \mathbf{n} = \frac{-\left(\frac{\partial h}{\partial x}\right)}{\sqrt{1+\left(\frac{\partial h}{\partial x}\right)^2+\left(\frac{\partial h}{\partial y}\right)^2}}\frac{\partial u}{\partial x} + \frac{-\left(\frac{\partial h}{\partial y}\right)}{\sqrt{1+\left(\frac{\partial h}{\partial x}\right)^2+\left(\frac{\partial h}{\partial y}\right)^2}}\frac{\partial u}{\partial y} + \frac{1}{\sqrt{1+\left(\frac{\partial h}{\partial x}\right)^2+\left(\frac{\partial h}{\partial y}\right)^2}}\frac{\partial u}{\partial z},$$

$$\frac{\partial v}{\partial n} = 0 = \nabla \mathbf{v} \cdot \mathbf{n} = \frac{-\left(\frac{\partial h}{\partial x}\right)}{\sqrt{1+\left(\frac{\partial h}{\partial x}\right)^2+\left(\frac{\partial h}{\partial y}\right)^2}}\frac{\partial v}{\partial x} + \frac{-\left(\frac{\partial h}{\partial y}\right)}{\sqrt{1+\left(\frac{\partial h}{\partial x}\right)^2+\left(\frac{\partial h}{\partial y}\right)^2}}\frac{\partial v}{\partial y} + \frac{1}{\sqrt{1+\left(\frac{\partial h}{\partial x}\right)^2+\left(\frac{\partial h}{\partial y}\right)^2}}\frac{\partial v}{\partial z}, \quad (1)$$

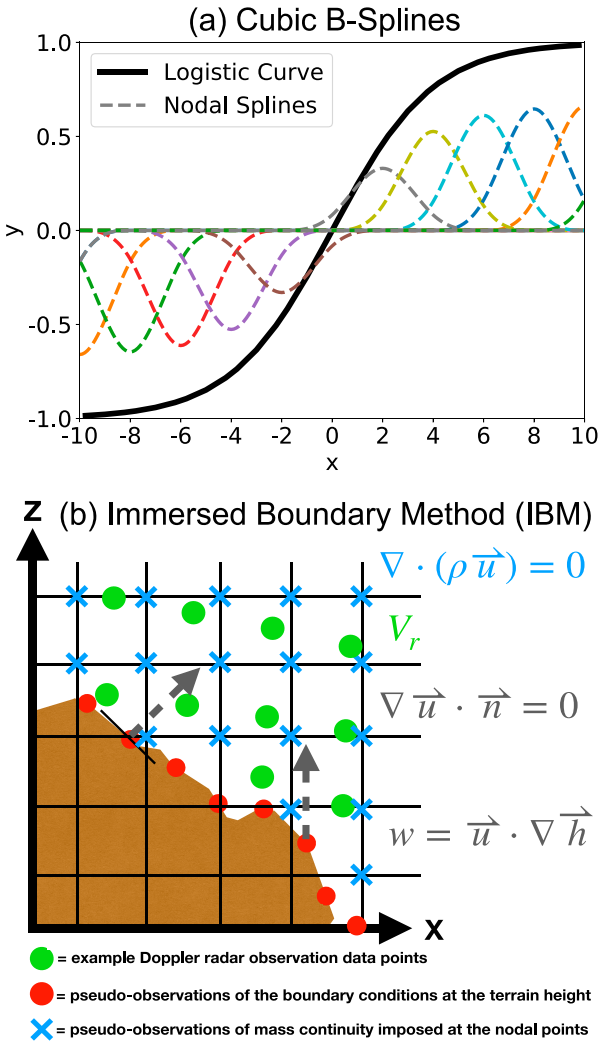

FIG. 1. (a) An example function and its component B-spline amplitudes. The thick black line is a logistic curve, and the dashed colored lines represent each individual B-spline at the nodal points that sum to represent the function. (b) A diagram illustrating the observational data points (green dots), pseudo-observations obtained from the two terrain boundary conditions (red dots and dashed lines), and pseudo-observations obtained from the mass continuity equation (blue cross). The background mesh grid lines represent the output analysis grid spacing.

$$w = u\frac{\partial h}{\partial x} + v\frac{\partial h}{\partial y}, \tag{2}$$

where **n** is the unit vector perpendicular to the boundary, u is the zonal wind, v is the meridional wind, w is the vertical wind, and h denotes the terrain height. The Neumann boundary condition is applied to u and v [Eq. (1)], whereas the Dirichlet boundary condition is used for w [Eq. (2)]. The Neumann boundary ensures that the total mass flux across the boundary is set to zero, preventing mass flux from penetrating the terrain. The Dirichlet boundary ensures that the vertical velocity at the terrain height is determined by the horizontal wind components u and v, thus accounting for the influence of topographic forcing. Given the correlation between the induced vertical velocity by topographic forcing and the terrain slope, the selection of an appropriate terrain map becomes crucial for resolving the desired scale of interest. This aspect will be further explored in section 4.

3. Data and sensitivity experimental setup

a. *Typhoon Chanthu (2021)*

Figure 2a depicts the track and intensity of Typhoon Chanthu. According to the Japan Meteorological Agency (JMA), the maximum wind speed of Chanthu was recorded as 115 kt (59 m s^{-1}) when the typhoon was located northeast of Luzon. Despite undergoing a weakening trend after reaching its peak intensity, Typhoon Chanthu exhibited intense eyewall convection over 50 dBZ as indicated by the radar composite reflectivity at 0530 UTC 12 September (Fig. 2c). The accompanying rainband, characterized by reflectivity values of 35–40 dBZ, made landfall in northern Taiwan. The spiral rainband exhibited a predominantly perpendicular orientation to the mountain slope, resulting in enhanced rainfall parallel to the ridge. Figure 2b shows the 24-h rainfall accumulation from 0800 UTC 12 September to 0800 UTC 13 September. A distinct band of enhanced precipitation, with a maximum accumulation exceeding 200 mm, is observed parallel to the snow mountain ridge. Interestingly, the minimum rainfall recorded over the Central Mountains ranges from 20 to 30 mm. These variations in rainfall accumulation and patterns suggest that topography plays a significant role in influencing the amount of precipitation, in addition to the influence of the typhoon circulation. The widespread orographic precipitation and strong wind speeds were captured by the Wufenshen (RCWF) and Shulin (RCSL) radar observations under an adequate dual-Doppler geometry (Table 2). Therefore, Typhoon Chanthu is selected as the case study for testing the improved technique.

b. *Dataset*

An OSSE was conducted for Typhoon Chanthu on 12 September 2021 when the typhoon's rainband made landfall in northern Taiwan, resulting in rainfall exceeding 50 mm within an hour in the mountainous region. OSSE studies are typically carried out to evaluate the effects of operational observing systems on observation-based value-added products and weather forecasts. The WRF simulation provides kinematic and thermodynamic variables with a physical understanding of the orographic effects on precipitating clouds and wind flow.

The WRF simulation uses version 4.1.3 (Skamarock et al. 2021). The Morrison double-moment scheme was utilized (Morrison et al. 2005). The Mellor–Yamada–Nakanishi–Niino level 2.5 (MYNN2.5) PBL scheme was adopted (Nakanishi and Niino 2009). The domains are configured as fixed triple-nested domains with two-way interaction for the second and third domains. The outermost domain has a horizontal grid spacing of 9 km, the second domain has a spacing of 3 km,

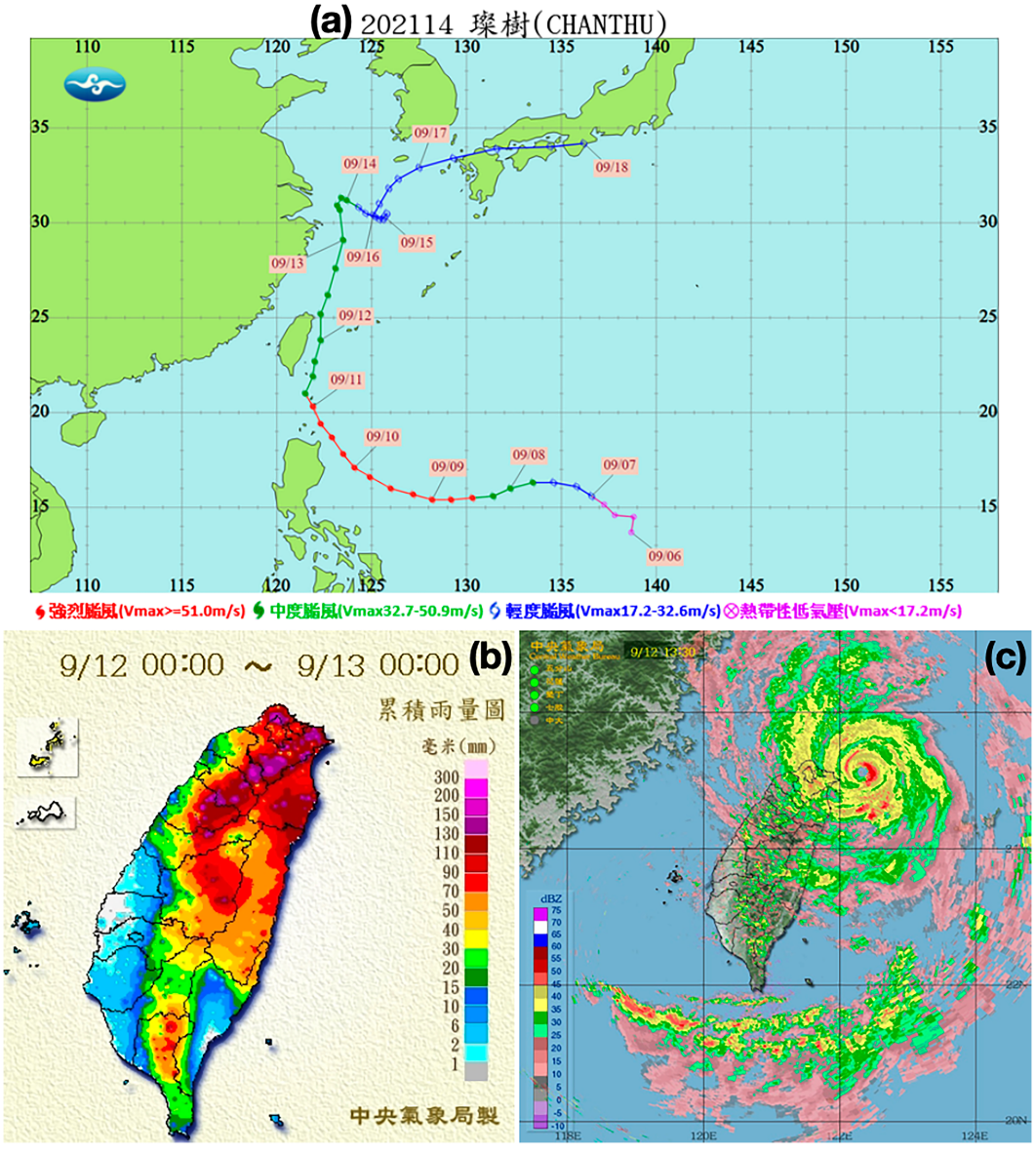

FIG. 2. (a) Typhoon Chanthu's track and intensity. (b) Twenty-four-hour rainfall accumulation from 0800 UTC 12 Sep to 0800 UTC 13 Sep. Time shown in the plot is in LST. (c) The composite radar reflectivity at 0530 UTC 12 Sep. All the figures were derived from the Central Weather Bureau Typhoon Database (https://rdc28.cwb.gov.tw/TDB/public/typhoon_detail?typhoon_id=202114).

and the innermost domain has a resolution of 1 km. The innermost domain has a horizontal grid spacing of 1 km and 51 sigma (σ) layers in the vertical. The initialization of this domain is based on the boundary conditions provided by the 3-km simulation. The WRF terrain height data have a horizontal resolution of 30 arc s, which corresponds to approximately 1 km horizontally. The terrain data are available at each grid point and have an averaged slope of 6×10^{-2} (∇h, unitless). In the WRF simulation, the native output is in the pseudopressure coordinate, resulting in a vertical grid that is stretched in physical space. The minimum vertical grid spacing in the WRF grid is approximately $\Delta z_{\min} \approx 23.22$ m, which is found at the peak of the hill. On the other hand, the maximum vertical grid spacing is approximately 644.46 m, occurring at a height of approximately $z \approx 5.2$ km.

The 1-km simulation was initialized following a 3-h run of the first and second domains, and output was produced at 15-min intervals. The innermost domain is designed to cover the northern part of Taiwan during the interaction of Typhoon Chanthu's rainband with the local topography. The simulation output at 0530:02 UTC September 12 is selected as the input data for the subsequent datasets described. As the focus of this study is on

TABLE 1. Sensitivity experimental setups designed to assess the performance of various configurations, including terrain boundary constraint, Doppler sampling limitations, and slope of terrain map. Note that the scientific notation of "1E-3" represents 1×10^{-3}, "6E-2" represents 6×10^{-2}, and so on. NE and DE stand for the pseudo-observation errors due to the Neumann boundary and Dirichlet boundary, respectively. The notations i and j represent the power of the exponents used with a base of 10.

Setup/labels	Reference ("truth")	CR-SIM: NE_iDE_j	Radar filter: NE_iDE_j	Radar filter: S_k
Data coordinates	WRF Model grid (x, y, σ)	WRF Model grid (x, y, σ)	Radar grid (azi, elev, range)	Radar grid (azi, elev, range)
Input data	u, v, w, T, q_v, ρ_a, ρ_m, Z_{hh}	Z_{hh}, V_d	Z_{hh}, V_d	Z_{hh}, V_d
Neumann error (i) i in [0, 1, 2, 3] (unitless)	1E-3	1E-3, 1E-2, 1E-1, 1E-0	1E-3, 1E-2, 1E-1, 1E-0	1E-3, 1E-2, 1E-1, 1E-0
Dirichlet error (j) j in [0, 1, 2, 3] (unitless)	1E-3	1E-3, 1E-2, 1E-1, 1E-0	1E-3, 1E-2, 1E-1, 1E-0	1E-3, 1E-2, 1E-1, 1E-0
Mean slope (k) (unitless)	6E-2	6E-2	6E-2	6E-2, 8E-2, 1E-1
No. of experiments	1	4×4	4×4	$3 \times 4 \times 4$

the impact of complex terrain on wind retrieval, the sampling time for the radar volume coverage pattern (VCP) and storm evolution are not considered.

Three types of OSSE datasets were generated:

1) REFERENCE ("TRUTH")

The WRF simulation is on a sigma coordinate, and the filtering length and actual resolving scale may slightly differ from the SAMURAI analysis. To ensure an equitable comparison, the sigma-level output data of the innermost WRF domain at 0530:02 UTC 12 September snapshot were loaded into SAMURAI. The reference analysis was generated by ingesting known data at WRF native coordinates with an observational error of 1 (unit corresponding to the variables), including a three-dimensional wind field (u, v, w), temperature, water vapor mixing ratio, dry air density, moist air density, and reflectivity. The terrain boundary error was set at 1×10^{-3} (unitless) for the analysis, as shown in the first column of Table 1.

2) CR-SIM

The Cloud-resolving Model Radar Simulator (CR-SIM; Oue et al. 2020) utilized the WRF simulation as input to generate equivalent radar reflectivity factor (Z_{hh}) and Doppler velocity (V_d) at the model grid. CR-SIM is a radar simulator designed to replicate multiwavelength, zenith-pointing, and scanning radar observations based on high-resolution cloud-resolving models. By employing the same microphysics scheme, CR-SIM can transform model variables into radar and lidar observables, facilitating direct comparisons between numerical weather model output and radar observations. The simulated radar observables account for sampling strategies, enabling the assessment of errors arising from sampling and uncertainties associated with multi-Doppler wind retrievals. This dataset at the WRF Model grid was generated by using the VCPs of the RCWF and RCSL radars, without considering time evolution (Table 2). The purpose of evaluating this dataset against the truth is to investigate Doppler errors in scenarios lacking direct vertical wind observations.

3) RADAR FILTER

The third dataset was generated by transforming the second dataset from the WRF Model grid to radar polar coordinates. This dataset, which incorporates more realistic radar characteristics, is evaluated against the first and second datasets to investigate radar geometry and sampling errors.

TABLE 2. The configuration of the RCWF and RCSL radars.

Radar	RCWF	RCSL
Radar location	25.071182°N, 121.781205°E	25.00°N, 121.4°E
Radar height (m)	765	298
Radar frequency (GHz)	3.0 (S band)	5.5 (C band)
Beamwidth	0.89	0.92
Range resolution (m)	250.0	250.0
Elevation angle	0.483 398 4, 0.878 906 2, 1.318 359, 1.801 758, 2.416 992, 3.120 117, 3.999 023, 5.097 656, 6.416 016, 7.998 047, 10.019 53, 11.997 07, 14.018 55, 16.699 22, 19.511 72	1, 2, 3, 4, 5, 6, 9.9, 14.6, 19.5, 24.5, 29.9
Time period (OSSEs)	Simulation output at 0530:02 UTC	
Time period (real data)	From 0530:16 to 0536:06 UTC	From 0527:24 to 0534:40 UTC

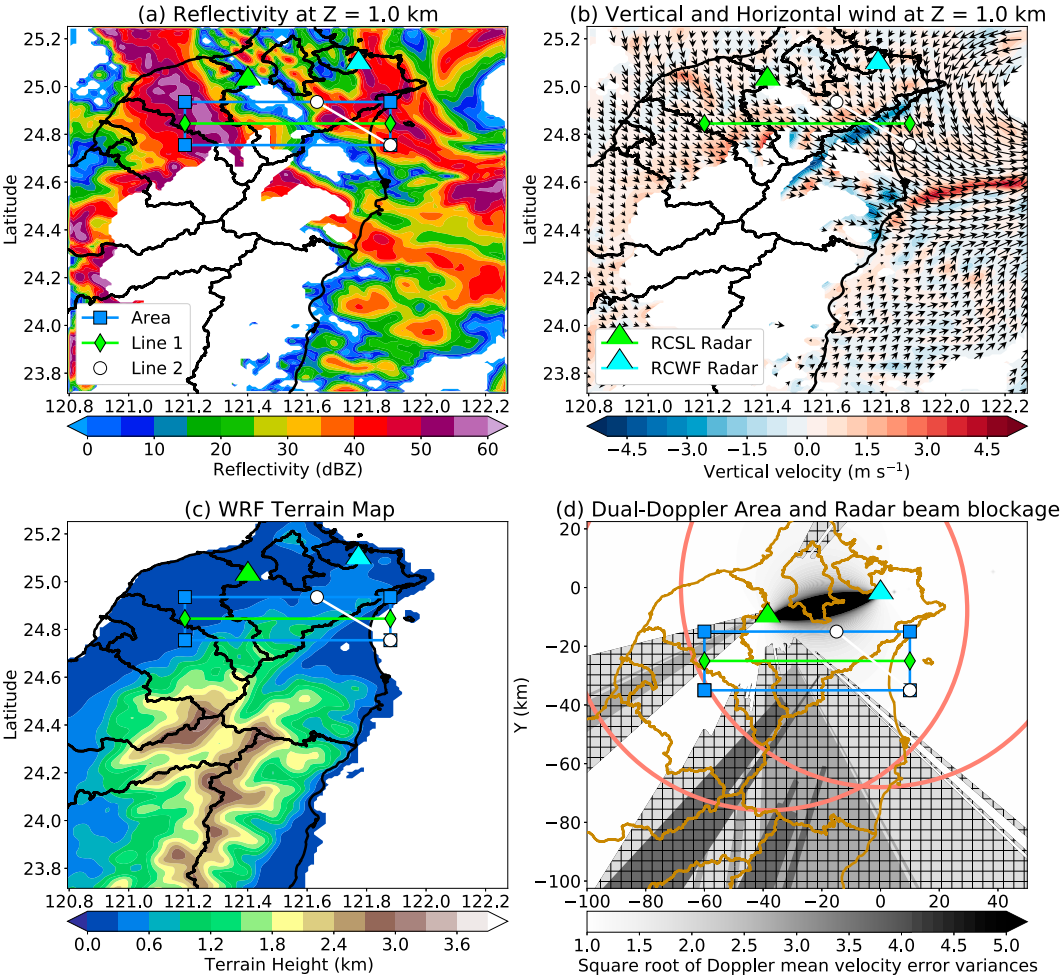

FIG. 3. Horizontal cross sections of (a) reflectivity and (b) vertical (shading) and horizontal wind (vectors) at 1-km altitude from the "truth." (c) WRF terrain map. (d) The effective dual-Doppler radar lobes. Large red circles represent the maximum observing range of RCSL and RCWF, respectively. The shading between the radars denotes the Doppler mean velocity error variances of the two radars, which are determined by the dual-Doppler radar beam geometry. The light gray contour with black hatches represents the RCSL radar beam blockage at the lowest elevation angle (1°), whereas the dark gray contour with black hatches represents the second lowest PPI (2°). The darkest gray contour with black hatches indicates the RCWF radar beam blockage at the lowest elevation angle (0.483°). The triangles denote the RCSL (green) and RCWF (cyan) radar locations, respectively. The blue box denotes the area where the accuracy of retrieval is assessed. The green and white lines denote two vertical cross sections that will be shown in section 4.

One caveat to note is that none of the datasets described above account for the beam blockage effect, which should be addressed in future work.

Figure 3 shows the "true" fields of reflectivity and vertical velocity, which are used to demonstrate the retrieval performance for the sensitivity tests. The white area in the horizontal cross section at 1 km (Figs. 3a,b) is a result of the terrain (Fig. 3c). To ensure an objective selection of an area of interest with suitable radar beam geometry and appropriate spatial resolution, the dual-Doppler lobes are depicted in Fig. 3d. Additionally, an accurate retrieval of the vertical velocity relies heavily on the dual-Doppler measurements, the mass continuity equation, and the assumed terrain boundary conditions. Therefore, selecting an effective area for dual-Doppler measurements is crucial in order to minimize errors caused by Doppler geometry, which ensures that the algorithm assumptions regarding the terrain boundary conditions can be evaluated with fewer concerns about other factors. An effective dual-Doppler measurement area is primarily determined by three factors: the minimum spatial resolution required to accurately resolve the phenomenon of interest, the maximum acceptable error in horizontal velocity, and the distance between the radars. Increasing the radar separation distance can enhance the accuracy of the two velocity components over a larger area, but it can lead to a degradation in spatial resolution near the radar locations. The dual-Doppler lobes can be defined by the intersection of the acceptable

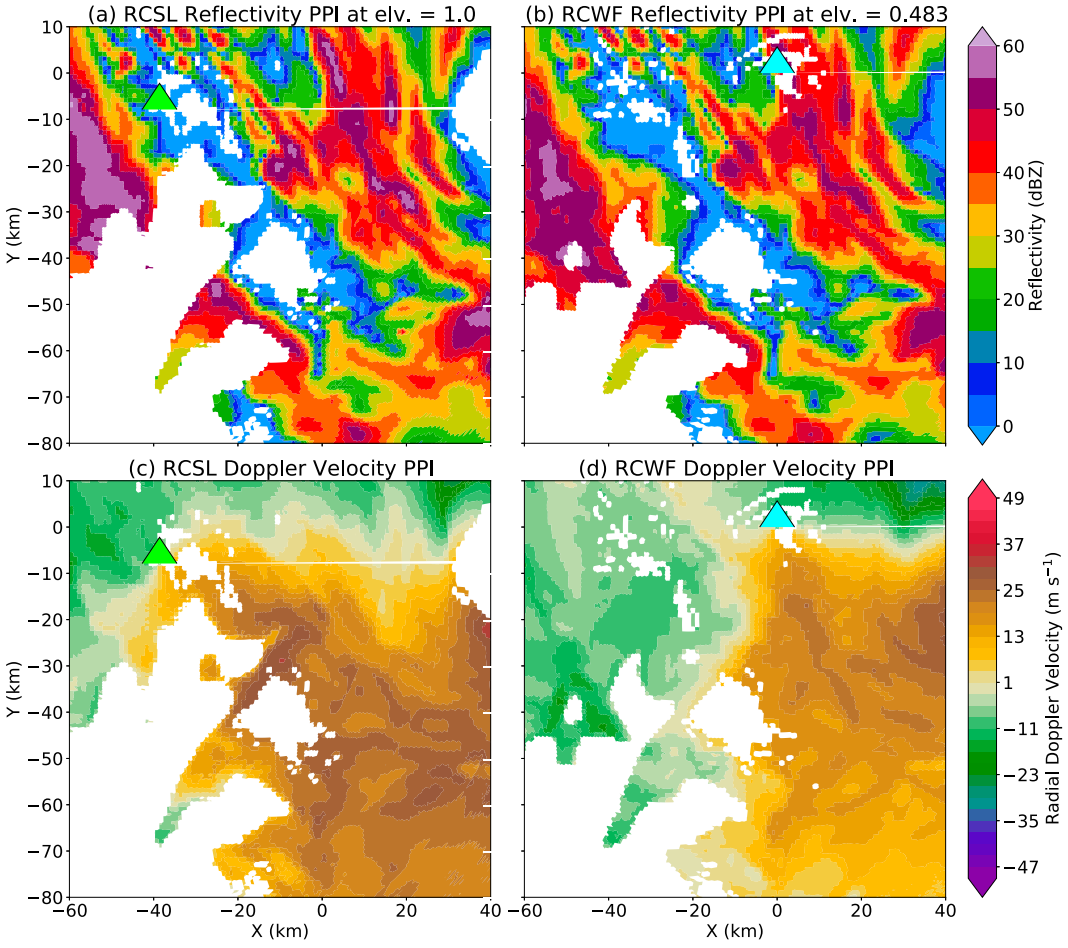

FIG. 4. PPI scans of radar reflectivity from (a) the RCSL at the elevation angle of 1° and (b) the RCWF at 0.483°. (c),(d) The Doppler velocity observed by the RCSL and the RCWF at the same elevation angles as (a) and (b), respectively.

velocity error variance and the maximum of the desired spatial resolution (Davies-Jones 1979; Friedrich and Hagen 2004). The maximum spatial resolution is determined by the radar separation distance and a selected cross-beam angle. In our case, the distance between the RCSL and RCWF is 39.26 km, yielding a fine resolution at close range. The beam crossing angle (β) is chosen to be 35° so that the resolution of the resulting merged data is ≈1 km. The horizontal wind solution is obtained by a geometrically weighted sum of the interpolated radial velocities. As the radial velocity measurements are sampled independently by different radars, the individual Doppler velocity variance can be used to estimate the error in the wind synthesis due to the geometry. The square root of the mean Doppler velocity variance derived from the two radars can be calculated to determine the potential error in the wind solution. In addition, partial or total beam blockage caused by mountains may limit the measurements from the low-elevation angles. The contours in Fig. 3d show the low-elevation beams where they are blocked by the surrounding terrain. Taking into account these factors, the resulting area for dual-Doppler analysis and selected cross sections with minimal beam blockage are shown in Fig. 3d.

To conduct realistic testing using the Taiwanese radar operational network and assess the overall wind retrieval for section 5 with real radar observations, we use the RCWF and RCSL radar configuration for the simulated radar measurements (Table 2). Note that in section 4, the results assume a static model output, where the radars collect data instantaneously based on their VCPs without any temporal evolution. All radar gate data points are at the same time step to reduce the uncertainty in retrieved winds caused by time discrepancies. Plan position indicator (PPI) of simulated reflectivity and Doppler velocity observed by the RCSL and RCWF are shown in Fig. 4 as an example.

c. *Assessment of accuracy*

The accuracy of the retrieved results against the true variables is evaluated using the spatial correlation coefficient (SCC) and the root-mean-square error (RMSE), including the horizontal wind field (u and v combined), vertical wind, and the first derivative of the wind field: divergence and vorticity, are computed (Liou et al. 2012):

$$\mathrm{SCC}(A) = \frac{(A_r - \overline{A_r})(A_t - \overline{A_t})}{\sqrt{(A_r - \overline{A_r})^2 (A_t - \overline{A_t})^2}}, \quad (3)$$

$$\mathrm{RMSE}(A) = \sqrt{\frac{\sum (A_r - A_t)^2}{M}}. \quad (4)$$

The subscripts "r" and "t" denote the "retrieved" and "true" quantities, M is the total number of grid points used in the computation, and $\overline{A}$ denotes the value of the domain average.

4. Sensitivity tests

In this section, we perform a series of sensitivity experiments to assess the impact of various factors on the accuracy of wind retrieval, including (section 4a) the prescribed strength of Neumann and Dirichlet boundary constraints, (section 4b) the smoothness of complex terrain slope, (section 4c) the algorithm assumptions of mass continuity and terrain boundary, and (section 4d) the grid spacing and Gaussian recursive filter setting. The purpose of each sensitivity test will be explained in its respective subsection. All the experiments herein are solely based on the input resampled observations and assumed boundary conditions. The first guess background wind field is set to be zero.

a. *Sensitivity of the prescribed strength of Neumann and Dirichlet boundary constraints*

Previous wind retrievals over complex techniques enforce the wind blocked and induced by topography to follow the terrain morphology according to the underlying physical understanding. Since SAMURAI offers the flexibility to adjust the strictness of the terrain boundary assumptions of surface impermeability and topographic forcing, this sensitivity experiment is conducted to explore the effectiveness of the assumption of boundary conditions compared to other methods that explicitly integrate any physical constraints. Table 1 displays the various experimental setups and their associated labels discussed in this subsection. The prescribed strength of the boundary constraint errors ranges from 1×10^{-3} ("1E-3") to 1×10^{-0} ("1E-0") and is applied to every data point at the terrain height. The prescribed strength of the constraint differs between the Neumann and the Dirichlet boundaries, but the mean slope is kept the same. This setup results in 16 experiments for the CR-SIM and radar-filter datasets, respectively, as shown in the second and third columns of Table 1.

Figure 5 shows the SCC scores of the CR-SIM and radar-filter datasets with various strengths of boundary errors. The CR-SIM experiments with different prescribed terrain boundary errors all outperform the radar-filter experiments in terms of the three-dimensional wind, divergence, and vorticity fields. The CR-SIM experiments show that relaxing the pseudo-observational errors provided by the boundary can retrieve a horizontal wind field similar to the reference data with an accuracy of up to 0.992. The average SCC score for the horizontal wind across all 16 sensitivity tests is 0.99, indicating a high fidelity of the horizontal wind retrieval from the Doppler velocity when sufficient data are available within the domain of interest. On the other hand, the retrieval of vertical wind is highly sensitive to the strength of imposing boundary conditions. If the Dirichlet error is relaxed to 1×10^{0}, which is approximately two orders higher than the averaged terrain slope (6×10^{-2}), the SCC score is less than 0.78 and shows no sensitivity to the order of the Neumann boundary error. When a strong Dirichlet boundary condition with an error of 1×10^{-3} is imposed, the SCC score drops below 0.76. However, setting the Dirichlet error to 1×10^{-1}, which is only one order higher than the averaged terrain slope, allows the SCC score to reach as high as 0.9. The CR-SIM results highlight the importance of setting the Dirichlet error to a similar order as the terrain slope map for accurate wind field reconstruction, whereas the Neumann error has less impact on the retrievals in our experiments when the data distribution and coverage are sufficient. The performances of the horizontal divergence and vertical vorticity are similar to the horizontal wind retrieval result and are relatively insensitive to the different orders of boundary errors (not shown). This experiment suggests that the Doppler error caused by the Doppler projection has minimal effect on the horizontal wind retrieval, but it has a more significant impact on the vertical wind due to its reliance on the mass continuity equation and topographic forcing assumptions.

The average SCC score for the radar-filter sensitivity experiments is 0.94 for horizontal wind retrieval and 0.73 for vertical wind retrieval. These scores are approximately 0.05 lower than the CR-SIM results, primarily due to the limited number of data points resulting from the designed VCP. Interestingly, the highest SCC score for the horizontal wind field is observed in the NE-1DE-1 experiment, whereas higher SCC scores for the vertical wind are mainly found in experiments with a 1×10^{-2} Dirichlet error, which is approximately the same order as the average slope of the terrain map. The shifting pattern compared to the CR-SIM experiments suggests that the strength of imposed terrain boundary conditions becomes more critical when there is less data close to the surface and sparse data distribution.

Considering the SCC and RMSE results (not shown), the NE-1DE-1 experiment demonstrates the best retrieval performance for this particular radar configuration and data distribution. Figure 6 illustrates a comparison of the same vertical cross section among the "truth," the CR-SIM NE-1DE-1 experiment, and the radar-filter NE-1DE-1 experiment (green line denoted in Fig. 3). A strong convective core with 60 dBZ at $X = -55$ km is associated with a 5 m s^{-1} updraft at $z = 5$ km. While the retrieved vertical velocities from both the CR-SIM and radar-filter experiments overestimate this specific updraft, the overall pattern closely resembles the reference. The zonal wind exhibits an enhanced upslope wind with divergence over the hill, accompanied by a downdraft down the hill and negative vorticity from $X = -30$ to 0 km. Although the CR-SIM and radar-filter experiments do not precisely capture the amplitude as expected due to Doppler errors, radar beam geometry, and limited data, they successfully resolve the physical and qualitative aspects of the feature of interest. It is important to note that in cases where data are sparse and the geometry of the dual-Doppler beams is poor (X = 0–5 km), there is a

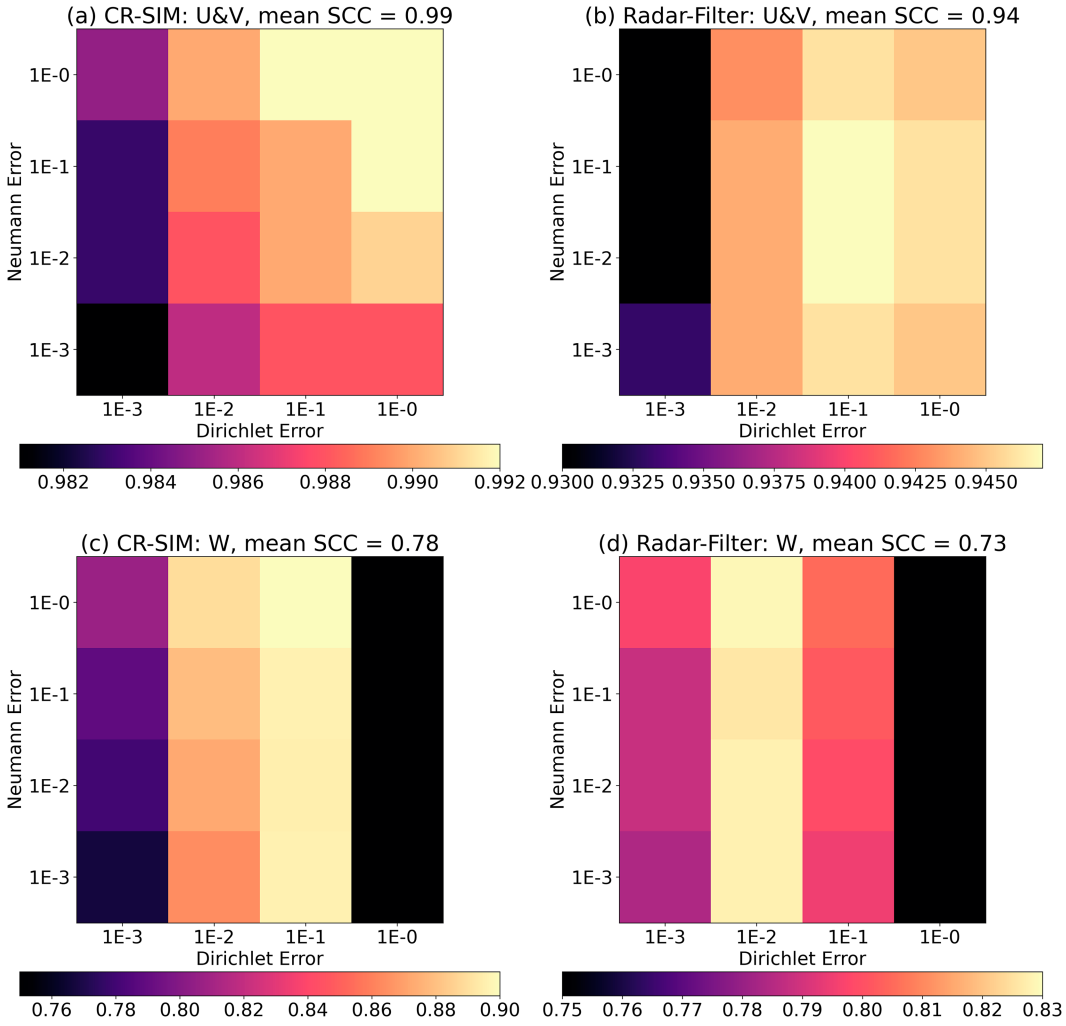

FIG. 5. The SCC scores of the wind field retrieved from (a),(c) the CR-SIM dataset and (b),(d) the radar-filter dataset are shown. In (a) and (b), the scores represent the horizontal wind, whereas in (c) and (d), the scores represent the vertical wind. The scores are computed using all the data points from the surface to 5 km within the blue box indicated in Fig. 3.

potential for the creation of artificial weak updrafts and downdrafts. Nonetheless, the overall analysis effectively captures our scale of interest.

Figure 7 shows another example of a vertical cross section across the snow mountain ridge, denoted by the white line in Fig. 3. The shallow convection is associated with positive vorticity and upslope wind, with a 2 m s^{-1} updraft and shallow convergence close to the ground. A jet with ≈32 m s^{-1} at $z = 3$ km is over the peak of the hill. A jet with a velocity of approximately 32 m s^{-1} at $z = 3$ km is located over the peak of the hill. Both the CR-SIM and radar-filter NE-1DE-1 experiments capture the pattern, although they slightly underestimate the downdraft magnitude at the lee side and overestimate the amplitude of the jet aloft and its position. The radar-filter NE-1DE-1 experiment exhibits a strong updraft at a height of 5 km (between $X = 0$ and 5 km), which is due to the absence of data close to the ground, leading to the dominance of the mass continuity equation in the retrieval of vertical velocity in that region. Nevertheless, the retrievals with terrain boundary implementations can capture the scale of interest and provide a good representation of mesoscale features.

To address the sensitivity of different prescribed strengths of the boundary constraints, Fig. 8 presents the impact of these constraints on the vertical velocity and vorticity patterns along the same vertical cross sections as shown in Figs. 6 and 7. When the Dirichlet boundary condition is relaxed, enhanced vertical motion is predominantly observed above 3 km in both cross sections. This behavior is dictated by the mass continuity assumption, which governs the retrieval pattern of vertical motion. On the other hand, the imposition of a strict Dirichlet boundary constraint enhances the influence of the terrain boundary on the vertical wind retrieval. This is evident in the retrieval's ability to capture the enhanced

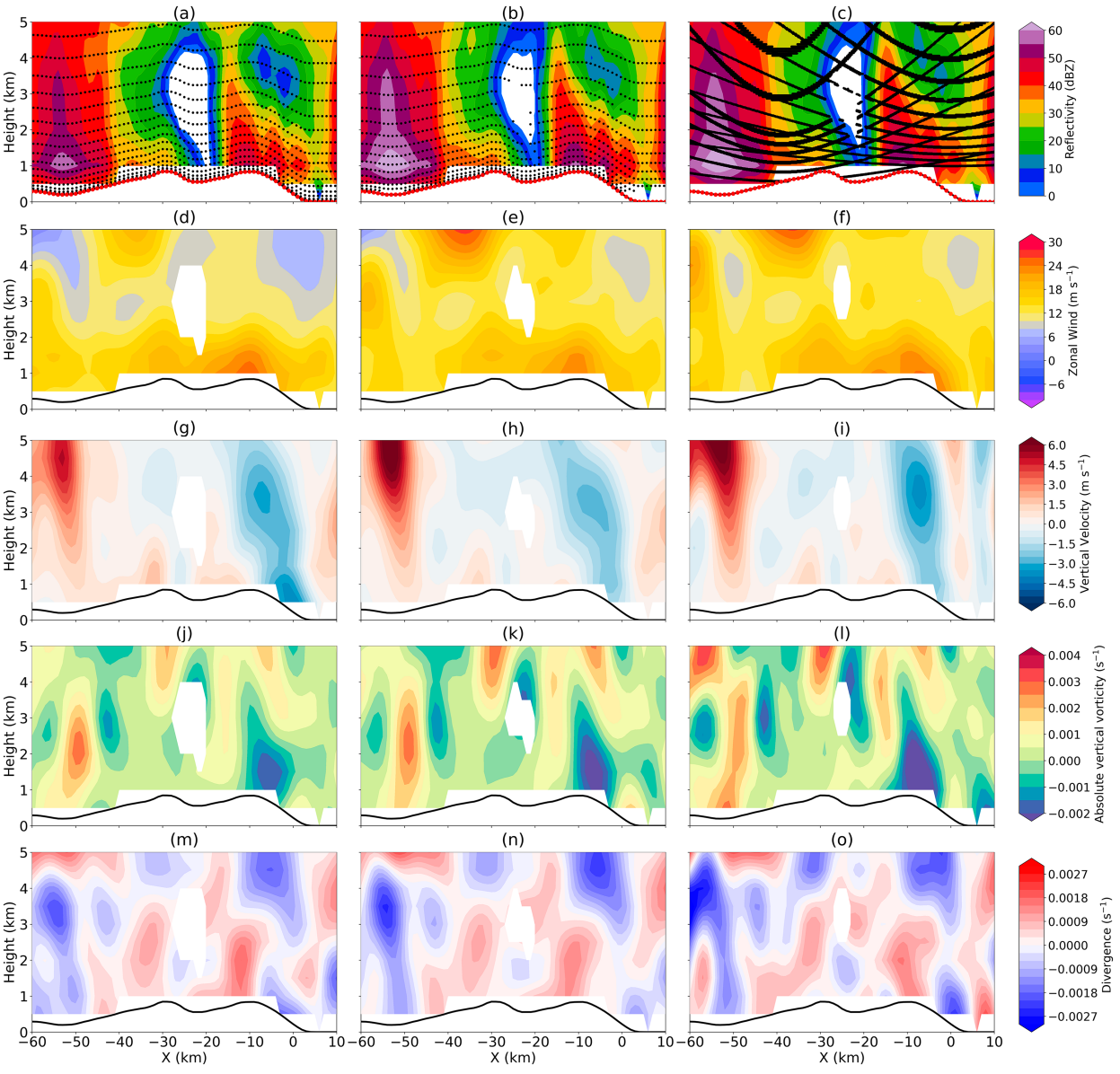

FIG. 6. Comparison of the (left) "truth," (center) CR-SIM: NE-1DE-1, and (right) radar filter: NE-1DE-1 retrieval output with the vertical cross sections of (a)–(c) reflectivity, (d)–(f) zonal wind, (g)–(i) vertical velocity, (j)–(l) absolute vertical vorticity, and (m)–(o) divergence. The vertical cross section is the green line denoted in Fig. 3. The black dot denotes the data distribution, and the red dot denotes the pseudo-observations imposed by the Neumann and Dirichlet boundary conditions at the terrain height. The black line denotes the topography.

downward motion locked to the terrain between −3 and 2 km, as seen in Figs. 7g and 8c, compared to the reference truth. The figure highlights that variations in the imposed Dirichlet boundary constraint result in notable changes in the vertical motion retrieval.

Regarding the absolute vertical vorticity, the retrievals from all experiments exhibit good agreement with the reference when there is sufficient data point coverage. The retrievals correctly identify regions of elongated positive vorticity from the surface to 3 km, positioned between two regions of negative vorticity, as seen in cross section 1 (Fig. 8b). Additionally, an enhanced negative vorticity region is identified on top of the peak between $X = -10$ and 0 km in cross section 1. Cross section 2 (Fig. 8) shows that the vorticity couplet close to the surface between $X = -15$ and 0 km is correctly identified, albeit with a slightly stronger amplitude compared to the reference. Although the amplitude is slightly off, the general vorticity pattern is well captured.

The sensitivity experiment results indicate the importance of prescribed boundary constraints in achieving an improved vertical wind structure. The error order of the prescribed boundary constraint depends on the density and distribution of data points near the surface. When data points are sufficient and close to the surface, the prescribed Neumann

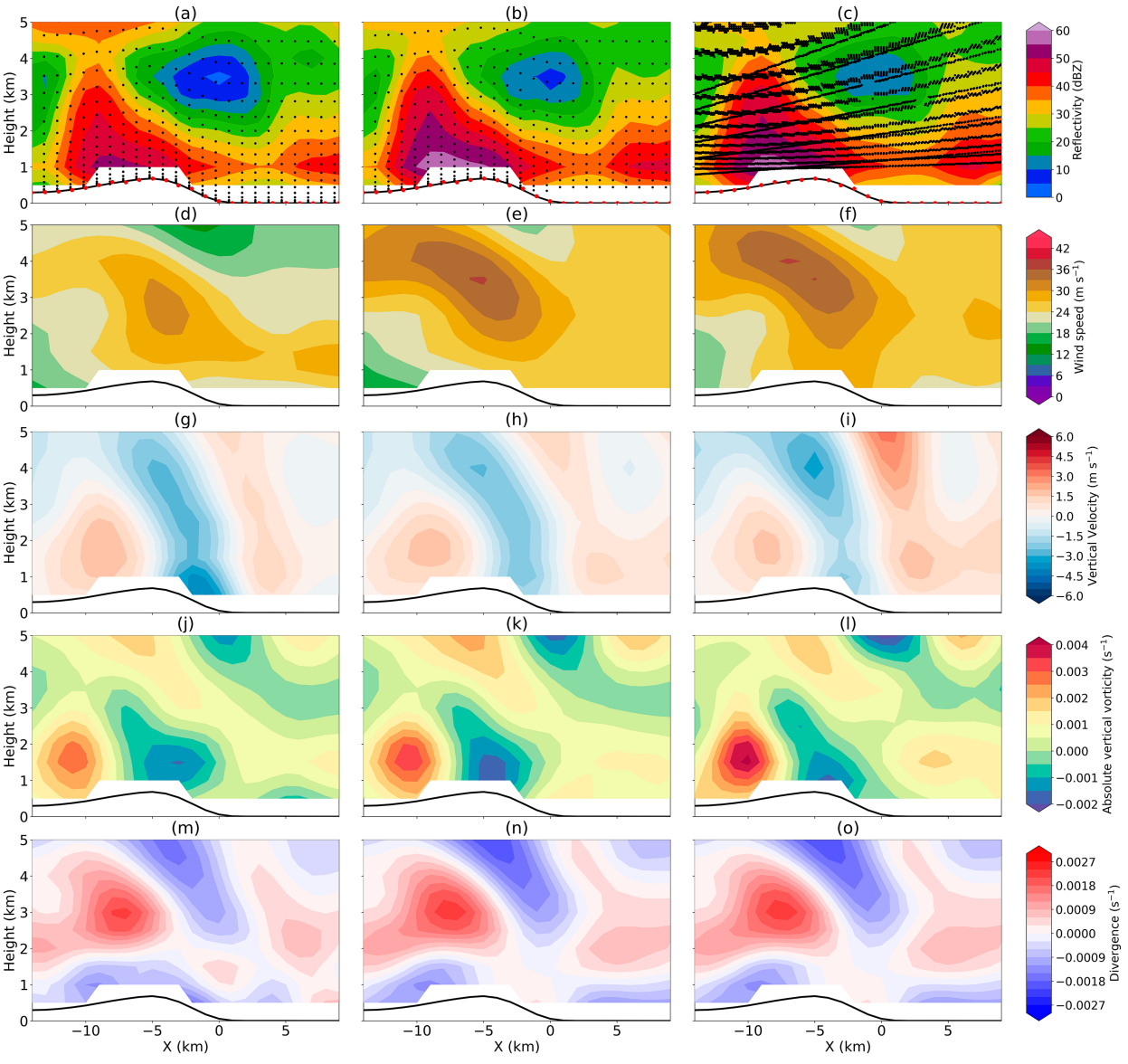

FIG. 7. As in Fig. 6, but for the vertical cross section along the white line denoted in Fig. 3.

boundary constraint may have a limited impact on the overall retrieval, whereas the Dirichlet boundary condition becomes more influential in the vertical wind retrieval. Although our results demonstrate that the best retrieval occurs when the prescribed boundary constraint has a similar order to the averaged terrain slope, it is important to note that this finding is specific to the examined radar geometry, and the exact numerical errors may vary in other scenarios.

b. *Sensitivity of the smoothness of complex terrain slope*

Orographic rainfall is sensitive to several factors, including mountain dimensions, cross-barrier flow, moist static stability, and microphysical processes. An idealized two-dimensional modeling study conducted by Colle (2004) found that the orographic precipitation is dependent on the dimensions of the mountain when the cross-barrier flow is less than 20 m s^{-1}. Kirshbaum and Durran (2005), using quasi-idealized numerical simulations, demonstrated that low-amplitude smooth topographic roughness can effectively act as prominent subscale peaks, triggering and organizing banded orographic precipitation. They also found that the bands created by isolated peaks can be sensitive to the location of those irregular peaks relative to the main ridge. In contrast, a recent study by Singh et al. (2021) suggests that using high-resolution topography in the model has the potential to reduce biases in the local-scale dynamics related to orographic features. Although our WRF simulation uses a terrain resolution of 30 arc s (approximately 1 km) with an average mean slope of 6×10^{-2} (S6E-2 experiment, Table 1), which represents the physical scale resolved by the model, it is still worthwhile to

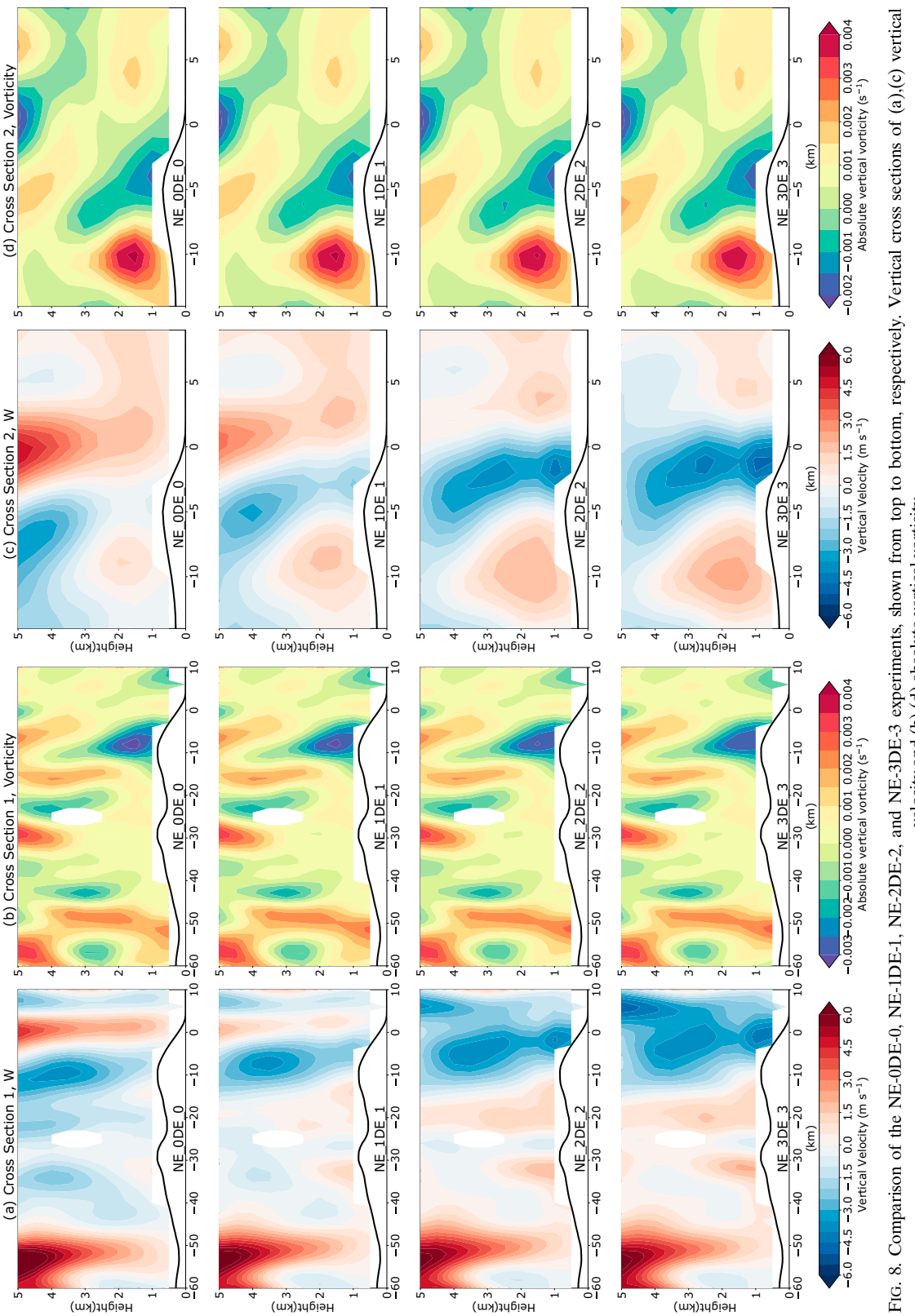

FIG. 8. Comparison of the NE-0DE-0, NE-1DE-1, NE-2DE-2, and NE-3DE-3 experiments, shown from top to bottom, respectively. Vertical cross sections of (a),(c) vertical velocity and (b),(d) absolute vertical vorticity.

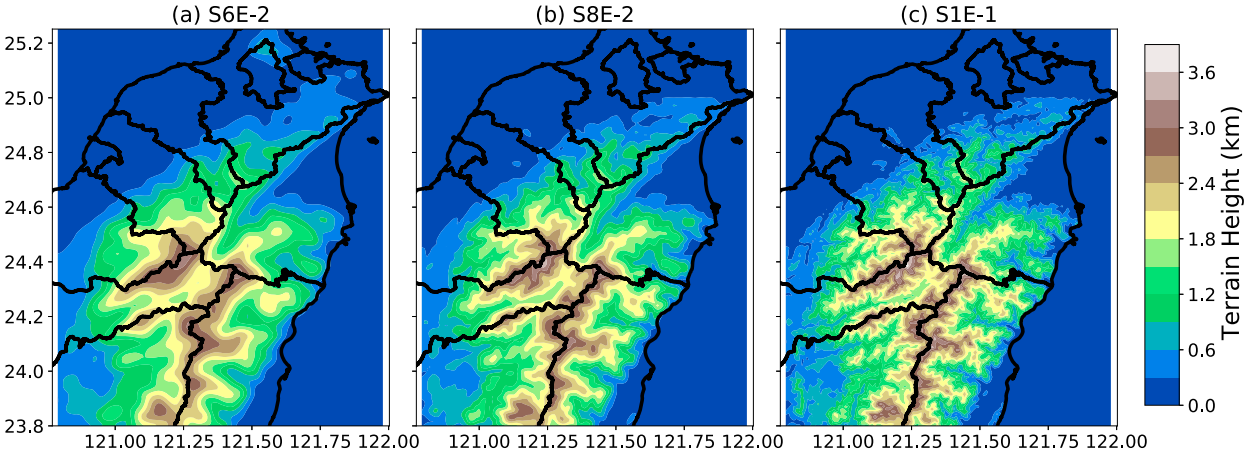

FIG. 9. Complex terrain in Taiwan with different average slopes: (a) S6E-2 (6×10^{-2}), (b) S8E-2 (8×10^{-2}), and (c) S1E-1 (1×10^{-1}).

investigate the sensitivity of the retrieval when using terrain maps with different degrees of smoothing and filtering.

The Advanced Spaceborne Thermal Emission and Reflection Radiometer Global Digital Elevation Map (ASTER GDEM) was generated using stereo-pair images collected by the ASTER instrument (U.S./Japan ASTER Science Team 2019). The ASTER GDEM data have a horizontal resolution of 1-arc-s (≈30 m) grid of elevation data. To match the scale of interest and reduce computational time, we employ two methods to align the 1-arc-s data with the 30-arc-s grid. The first method involves applying a fast Fourier transform (FFT) to the ASTER GDEM data, removing wavenumbers lower than 33, and preserving approximately 1-km features. This terrain map exhibits an averaged terrain slope of 8×10^{-2} (S8E-2 experiment), closely resembling the terrain map in the WRF simulation while retaining some irregular peaks. The second method involves subsampling the ASTER GDEM data and performing nearest neighbor interpolation from high resolution to low resolution. This approach preserves most of the peaks with steeper slopes compared to other methods, resulting in a terrain map with an averaged terrain slope of 1×10^{-1} (S1E-1 experiment).

Figure 9 depicts the complex terrain with varying terrain slopes, and the details of the experimental setup can be found in Table 1. Among the three experiments, the S6E-2 experiment exhibits the smoothest terrain, whereas the S1E-1 preserves the most intricate features. The sensitivity test in this section also varies the strength of Neumann and Dirichlet boundary constraints to explore the relationship between the boundary conditions and terrain slope features. The sensitivity test in this section also investigates the impact of varying the strength of Neumann and Dirichlet boundary constraints under different terrain slope features on the retrieval results.

Figure 10 shows the RMSE results from the sensitivity experiments. Using the terrain slope corresponding to the simulation yields the lowest RMSE for the wind field as expected, since the original terrain map provides a better representation of the phenomenon at the desired scale. Among the three experiments, the S1E-1 retrieved wind exhibits the highest RMSE. In the S1E-1 experiment, the horizontal and vertical retrievals show the best performance when the Dirichlet constraint is prescribed with a 1×10^{-1} error. The S8E-2 experiment demonstrates a similar pattern to the S1E-1 experiment but with a lower RMSE. Notably, all the experiments conducted here exhibit a lower sensitivity to the Neumann boundary error, likely due to an appropriate Doppler radar geometry setup in the region of interest.

Figure 11 displays the vertical cross sections obtained from the S6E-2, S8E-2, and S1E-1 experiments, with a Neumann and Dirichlet boundary error of 1×10^{-1}. The overall patterns are similar among the three experiments and consistent with the model in general, aligning with the findings of Kirshbaum and Durran (2005). In the experiments with steeper and more detailed terrain, an enhanced downdraft near the terrain peak (between $X = -8$ and -3 km) is observed in the S8E-2 and S1E-1 experiments, with the S1E-1 experiment exhibiting a magnitude of up to 5.5 m s^{-1}. The divergence field indicates an intensified convergence at a height of 4.5 km between $X = -8$ and -3 km in the S8E-2 and S1E-1 experiments, suggesting that the influence of the steepness of the terrain slope can extend to higher altitudes, rather than being confined to the lower levels. These sensitivity experiment results emphasize the importance of using a terrain map that aligns with the desired scale of interest for accurate wind field reconstruction.

c. *Sensitivity of the algorithm assumptions of mass continuity and terrain boundary*

The traditional method for retrieving vertical air motion involves solving the integral mass continuity equation by integrating upward from the bottom level and/or downward from the top level (Ray et al. 1980; Protat and Zawadzki 1999). This approach requires an estimation of horizontal wind divergence at each level, and errors in horizontal wind divergence can propagate and accumulate throughout the column, leading to larger errors in the retrieved vertical velocity. The variational approach has been shown to be less sensitive to the specification of boundary conditions for vertical velocity

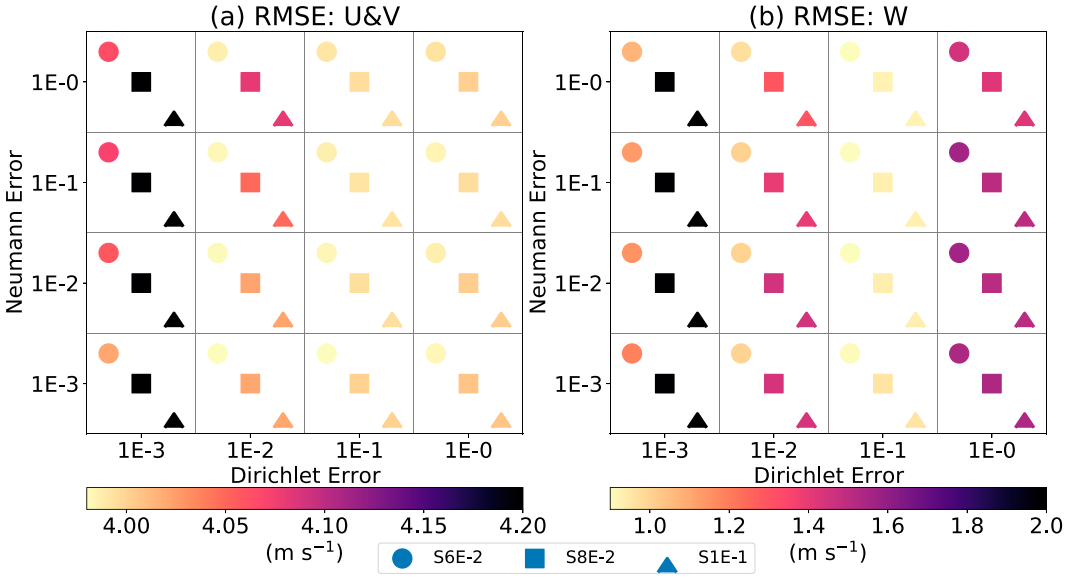

FIG. 10. Scatterplot showing the RMSE of the (a) horizontal wind and (b) vertical wind from the S6E-2, S8E-2, and S1E-1 experiments with different specified terrain boundary condition errors. The color shading of the dots represents the magnitude of the RMSE.

retrieval (Gao et al. 1999; Potvin et al. 2012a), but the sensitivity of vertical wind retrieval regarding the mass continuity and the terrain boundary constraints have not been explored before. In this experiment, we explore the algorithm assumptions of the mass continuity equation and terrain boundary conditions through three types of experiments: with the mass continuity, no terrain boundary condition (WM-NT), NW-WT, and with mass continuity, with terrain boundary condition (WM-WT). The experimental configuration is detailed in Table 3.

Figure 12 shows the vertical cross section 1 obtained from the experiments. First of all, the WM-NT experiment exhibits artificial wind below the terrain, characterized by weak zonal wind and vertical velocity near the ground. The occurrence of artificial wind below the terrain is a result of interpolating the missing data area to $z = 0$ km using cubic B-splines and the Gaussian recursive filter in order to satisfy the boundary condition that the vertical wind is 0 m s^{-1}. Second, the WM-NT result shows a similar pattern as the other two in the horizontal wind field, vorticity, and divergence when the retrieval is above the terrain. The zonal wind near the terrain height, between $X = -5$ and 5 km, reaches speeds up to 30 m s^{-1}, whereas the WM-WT retrieval shows zonal wind of only 25 m s^{-1}. Third, the lack of terrain boundary constraints has a significant impact on the retrieval of vertical wind. The WM-NT experiment produces four strong updrafts with an approximate magnitude of 6 m s^{-1} and one downdraft with a magnitude of 5 m s^{-1} peaking at a height of 3.5 km. While the WM-NT experiment captures the two uphill updrafts (one between $X = -40$ and -30 km and the other between $X = -20$ and -10 km), their amplitudes are excessively strong, and the vertical motion extends too far upward compared to the reference. In the NM-WT experiment, the horizontal wind, vorticity, and divergence fields are in good agreement with the WM-WT experiment, similar to the WM-NT case. The enhanced vertical velocity is closely coupled with the terrain, and the vertical velocity remains close to zero above a height of 4 km.

Figure 13 presents the results of vertical cross section 2. The overall findings are consistent with those in Fig. 12, but one notable feature is the presence of a weak updraft (between -10 and -5 km) associated with upslope wind, which is not captured by the WM-NT experiment. These unresolved wind features along the slope arise from the assumption of $w = 0$ m s^{-1} at $z = 0$ km. This assumption leads to strong divergence and the formation of a low-level jet below the terrain, so a compensating downdraft aloft counteracts the upward motion. In the NM-WT experiment, a much stronger downdraft of up to -6 m s^{-1} is observed, which is shifted downhill and closer to the surface compared to the WM-WT experiment. These experiments highlight the necessity of considering the assumptions of the mass continuity and the terrain boundary condition to obtain an accurate and realistic representation of the vertical wind field.

d. Sensitivity to the grid spacing and Gaussian recursive filter setting

In principle, a minimum of five grid points is required to represent a wave on a grid to ensure that the resolvable wave is on a scale of 2 times the data spacing Δn (Koch et al. 1983). To accurately represent a resolvable wavelength, Δx should then not exceed half of Δn. Regarding the lower limit, it is not recommended to have an overly fine grid spacing, as calculations of derivative quantities become sensitive to the grid length and the computations become more expensive. Therefore, the empirical ratio between the grid spacing (Δx) and

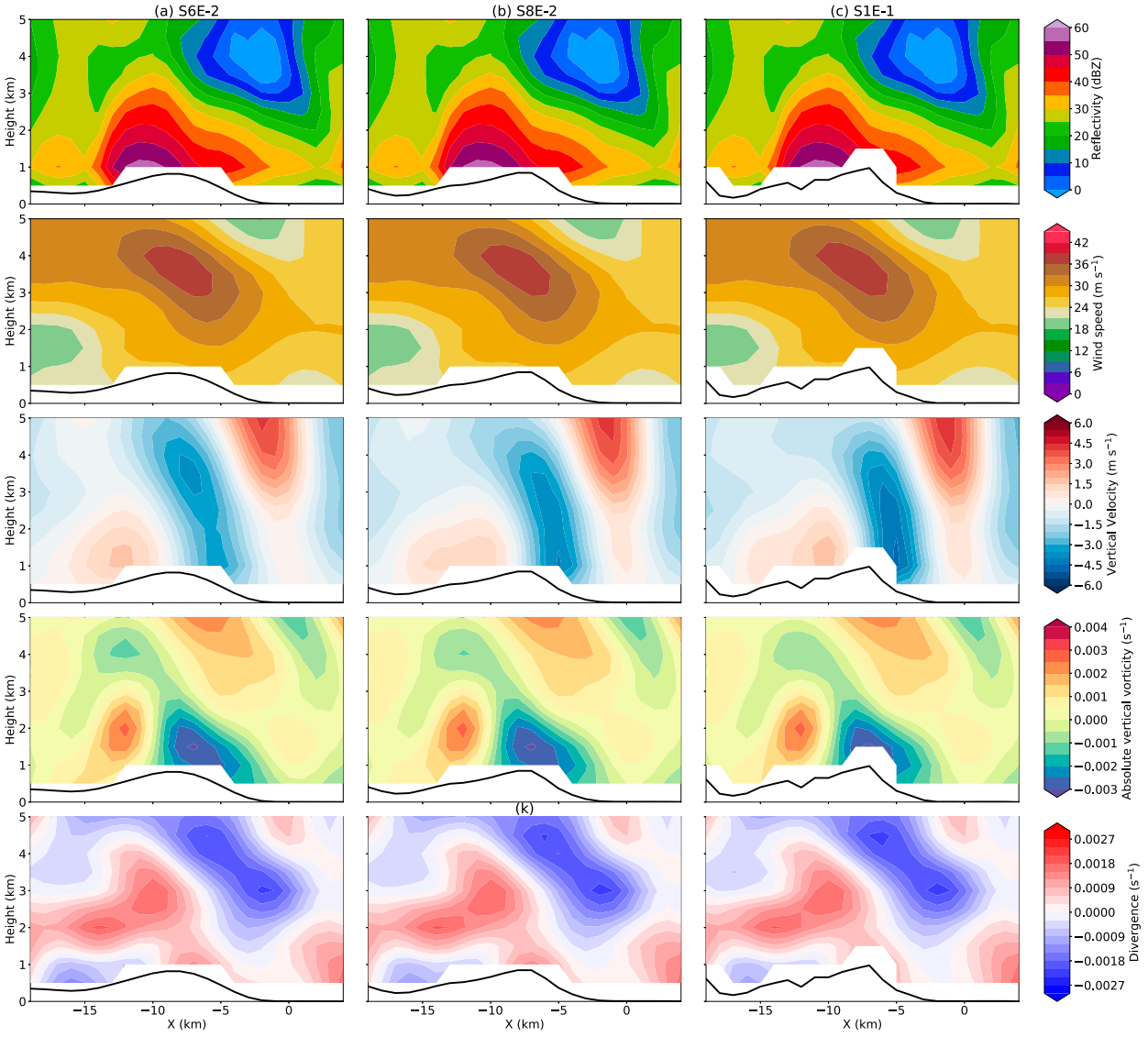

FIG. 11. Same vertical cross section as shown in Fig. 7, but for the (a) S6E-2, (b) S8E-2, and (c) S1E-1 experiments with a 1×10^{-1} error for the Neumann and Dirichlet boundary conditions. The black line represents the terrain height along the cross section.

the data spacing (Δn), denoted as $\Delta x/\Delta n$, falls within the range from 1/3 to 1/2, as suggested by the Barnes objective technique (Koch et al. 1983). In SAMURAI, the resolved wind field is a function composed of finite elements. The grid spacing determines the minimum spatial scale resolved by the cubic B-spline function. The Gaussian filter produces a Gaussian response to a point observation but can dampen the amplitude of lower wavelengths and make the retrieval less sensitive to noise. The Gaussian filter setting determines the length scale in grid points, and a higher value can result in larger spatial influence of the observations and additional smoothing. Choosing an appropriate combination of grid spacing and filter settings is crucial to retrieve the best representation of the desired scale of interest. For example, since our scale of interest is approximately 4 km, the grid spacing can be set to 1 km and the Gaussian filter is set to 4. Alternatively, the grid spacing can be set to 2 km and the Gaussian filter is set to 2. Both settings can provide a good representation of the scale of interest with slightly different results, and features and noise with wavelengths less than 4 km will be damped.

Observations inherently include a certain level of noise, and applying a Gaussian filter can help smooth out this noise. For a well-resolved Doppler geometry, the uncertainty in the wind field should be less than 2 m s^{-1} (Hildebrand et al. 1996). To explore the sensitivity of the grid spacing and Gaussian recursive filter setting, we add Gaussian noise with one standard deviation of the Doppler velocity for the WRF input data, considering the subgrid-scale turbulence and Doppler velocity instrument noise. A sensitivity test of

TABLE 3. Configuration of different experimental setups for testing the sensitivity of mass continuity and the terrain boundary conditions for three-dimensional wind retrieval. The prefix WM (with the mass continuity) or NM (no mass continuity) indicates whether mass continuity is activated or not. Similarly, the prefix WT (with the terrain boundary condition) or NT (no terrain boundary condition) indicates whether the terrain boundary condition is activated or not.

Name	Mass continuity, error	Terrain boundary, (Neumann error, Dirichlet error)
WM-NT	Yes, 1	No, (—, —), $w = 0$ m s^{-1} at $z = 0$ km
NM-WT	No, —	Yes, (1×10^{-1}, 1×10^{-1})
WM-WT	Yes, 1	Yes, (1×10^{-1}, 1×10^{-1})

different grid spacing and the length of filter setup is shown in Table 4.

Figure 14 displays the results from each sensitivity experiment compared to the WRF simulation direct output. The Grid05Filter222 configuration is designed to resolve features at a scale of approximately 1 km. The Grid05Filter222 analysis retains more detail, but the overall retrieval is noisy (Fig. 14b), particularly for the vorticity and divergence fields because the derivative of the wind field is more sensitive to the wind gradient. The Gaussian filter is set to two nodes, which is not sufficiently strong to suppress the noise. The RMSE of the vertical velocity is 0.77.

The Grid05Filter442 and Grid10Filter222 configurations achieve a similar horizontal resolved scale of 2 km. The Grid10Filter222 configuration retains more details, whereas the Grid05Filter442 analysis appears smoother due to the stronger Gaussian filter that effectively suppresses more noise (Figs. 14c,d). Both the Grid05Filter442 and Grid10Filter222 configurations can capture a similar pattern to the WRF output with detailed structures and reduced noise compared to the Grid05Filter222 results. However, there are still some artificial enhanced wiggles of features due to the mismatch in the resolved scale.

Overall, the Grid10Filter442 configuration achieves a horizontal-scale resolution of 4 km which provides the best representation of the scale of interest (Fig. 14e). Among all the tests, the Grid10Filter442 configuration exhibits the minimum RMSE for both the horizontal and vertical wind, with values of 1.85 and 0.76 m s^{-1}, respectively.

Since the quality and sampling of Doppler velocity strongly influence the spatial resolution, resolved scales, and accuracy of the wind and terrain boundary constraint, it is not possible to provide a specific recommendation for filter length, grid spacing, strength of the terrain boundary constraint, and the order of the terrain slope that applies universally to all cases. Based on the given sampling and theoretical understanding, setting the grid spacing to 0.5 km is more appropriate to resolve the detailed structure (Koch et al. 1983; Ooyama 1987, 2002). However, in order to align with the resolving scale of the WRF Model, a similar horizontal resolved scale of 4 km is considered more appropriate. Results from the OSSE experiments indicate that a 0.5-km horizontal grid spacing and a Gaussian recursive filter length of 4 times the grid spacing in the horizontal direction yield the most detailed structures. On the other hand, a 1-km horizontal grid spacing and the same filter length provide higher confidence in capturing both the structure and magnitude of dominant mesoscale features. The sensitivity experiments demonstrate that different analysis settings entail an inherent trade-off between level of detail and pointwise accuracy. Therefore, the choice of settings must be carefully evaluated on a case-by-case basis, and their interpretations should be made accordingly when drawing scientific conclusions.

5. Application of real data

This section demonstrates the applicability of the improved SAMURAI approach using real data from Typhoon Chanthu (2021) observed by the RCSL and RCWF radars. The radar configurations and settings are shown in Table 2. The use of real data introduces additional challenges due to incomplete data coverage and beam blockage, especially near the ground and on the lee side of hills in mountainous regions. Furthermore, the quality of the wind field is dependent on the Doppler velocity quality and scanning geometry of the radars. Considering the sensitivity tests performed on the OSSE experiments and the limitations of real radar observations, the analysis was performed using pseudo-observations with Neumann and Dirichlet boundary conditions with a prescribed pseudo-observational error of 1×10^{-1}, a terrain map with a mean slope of 6×10^{-2}, a horizontal grid spacing of 1 km, a vertical grid spacing of 0.5 km, and a Gaussian recursive filter length of 4Δ nodal spacing in the horizontal dimension and 2Δ spacing in the vertical dimension.

The radar sweep files were processed using the Lidar Radar Open Software Environment (LROSE) software (Bell et al. 2021) and the National Center for Atmospheric Research (NCAR) SoloII software. These processing steps involved correcting Doppler velocity aliasing, as well as removing nonmeteorological echoes and noise. After the editing process, the sweep files were converted to the CfRadial format in the native radar polar grid, which were used as input for further analysis.

Figure 15 shows the horizontal cross sections of the SAMURAI analysis. A rainband moving inland with reflectivity values over 50 dBZ suggests intense precipitation on the uphill side of the terrain. Interestingly, an elongated, thin band of downward motion parallel to the mountain range (between 121.6° and 121.8°E, between 24.7° and 24.9°N) is found at $z = 1$ km, collocated with a band of positive vorticity. Upward motion is most dominant on the windward side of the mountain range and increases with height, while the confidence in the wind retrievals along the baseline is lower. Considering the dual-Doppler lobes and the scarcity of data, our focus is on a specific vertical cross section indicated by the white line, which corresponds to an area with sufficient coverage of the dual-Doppler radar beams. This cross section is parallel to the rainband's horizontal wind flow and is perpendicular to the mountain ridge, which makes it easier to assess if the retrieved wind field is physically realistic.

Figure 16 illustrates the vertical cross section of reflectivity, wind flow, vorticity, and divergence. In Fig. 16a, a shallow reflectivity echo with a value of 50 dBZ is observed at 1-km

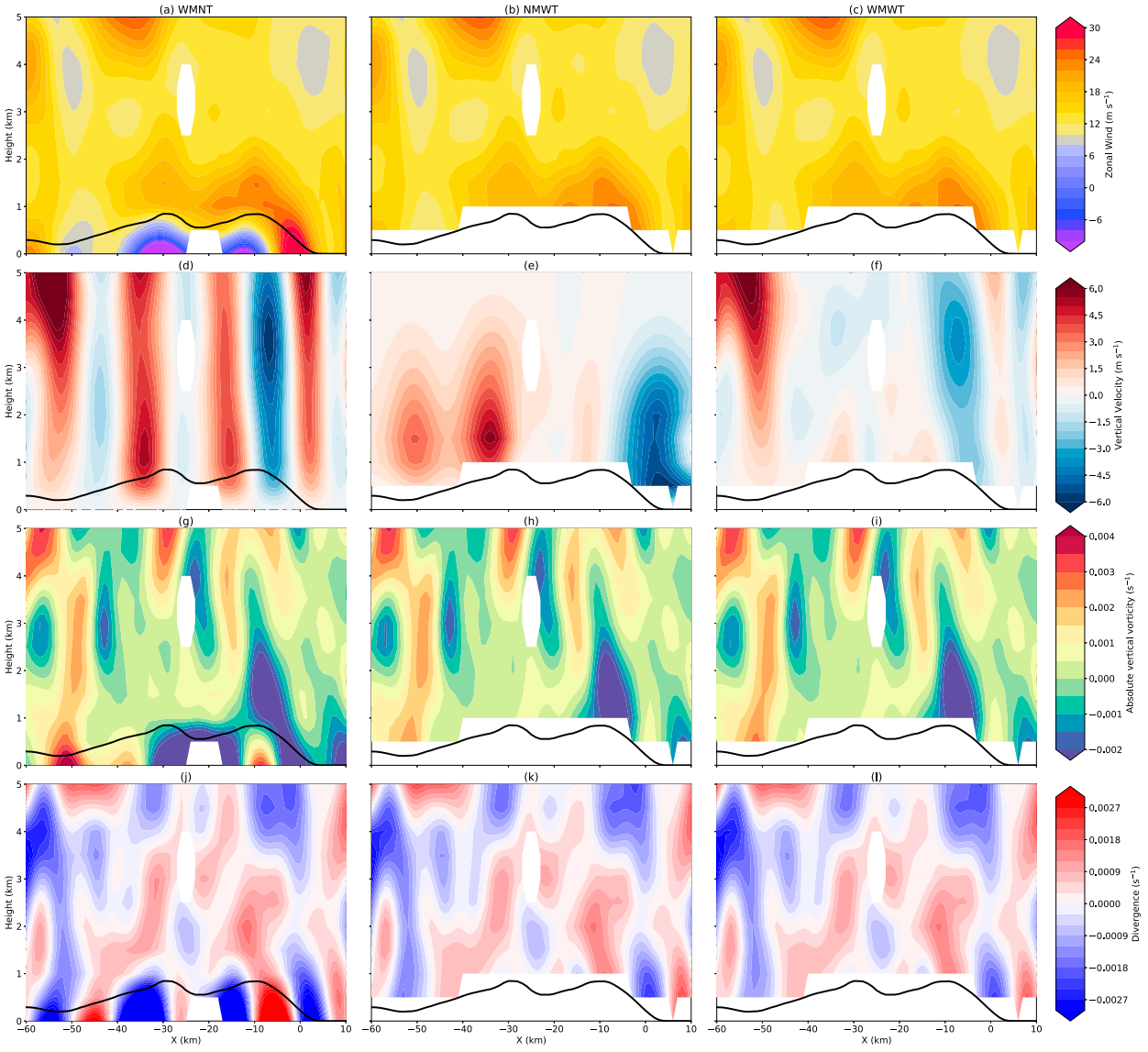

FIG. 12. Same vertical cross section as shown in Fig. 6, but for the (a) WM-NT, (b) NM-WT, and (c) WM-WT experiments, displaying zonal wind, vertical velocity, absolute vertical vorticity, and divergence from top to bottom. The black line represents the terrain height along the cross section.

height on the windward side. This enhanced echo extends up to 6-km height (between $X = -20$ and -16 km). Within this region, the shallow stratiform precipitation near the ground is associated with upslope wind and divergence. At 4-km height, there is convergence as shown in Fig. 16e, accompanied by upward motion aloft and downward motion below, as depicted in Fig. 16c. These findings align with the expected stratiform heating profile.

Between $X = -16$ and -12 km, as the wind flow ascends the terrain, it induces upward motion with a magnitude of 2 m s^{-1}. This upward motion is accompanied by negative vorticity (-0.0012 s^{-1}) and weak divergence near the terrain. The upward motion continues vertically and reaches its maximum amplitude of 5 m s^{-1} at a height of 5 km. At this height, the vertical velocity is associated with positive vorticity, convergence below, and divergence aloft. The cross-barrier wind flow reaches its maximum at the mountain peak, exceeding 25 m s^{-1}, and decreases in the lee. Estimates of the mountain Froude number (Smith and Barstad 2004) are greater than one, indicating that the airflow successfully ascends over the mountains without significant blockage [see Cha (2023) for detailed calculation]. The results of our radar analysis are consistent with the general theoretical understanding of orographic precipitation. The flow in the lee is characterized by downward motion, positive vorticity in close proximity to the topography, and slight convergence above the ground. A comprehensive analysis of the evolution of Typhoon Chanthu's rainband and its interaction with topography is beyond the scope of the current study and will be addressed in a future study.

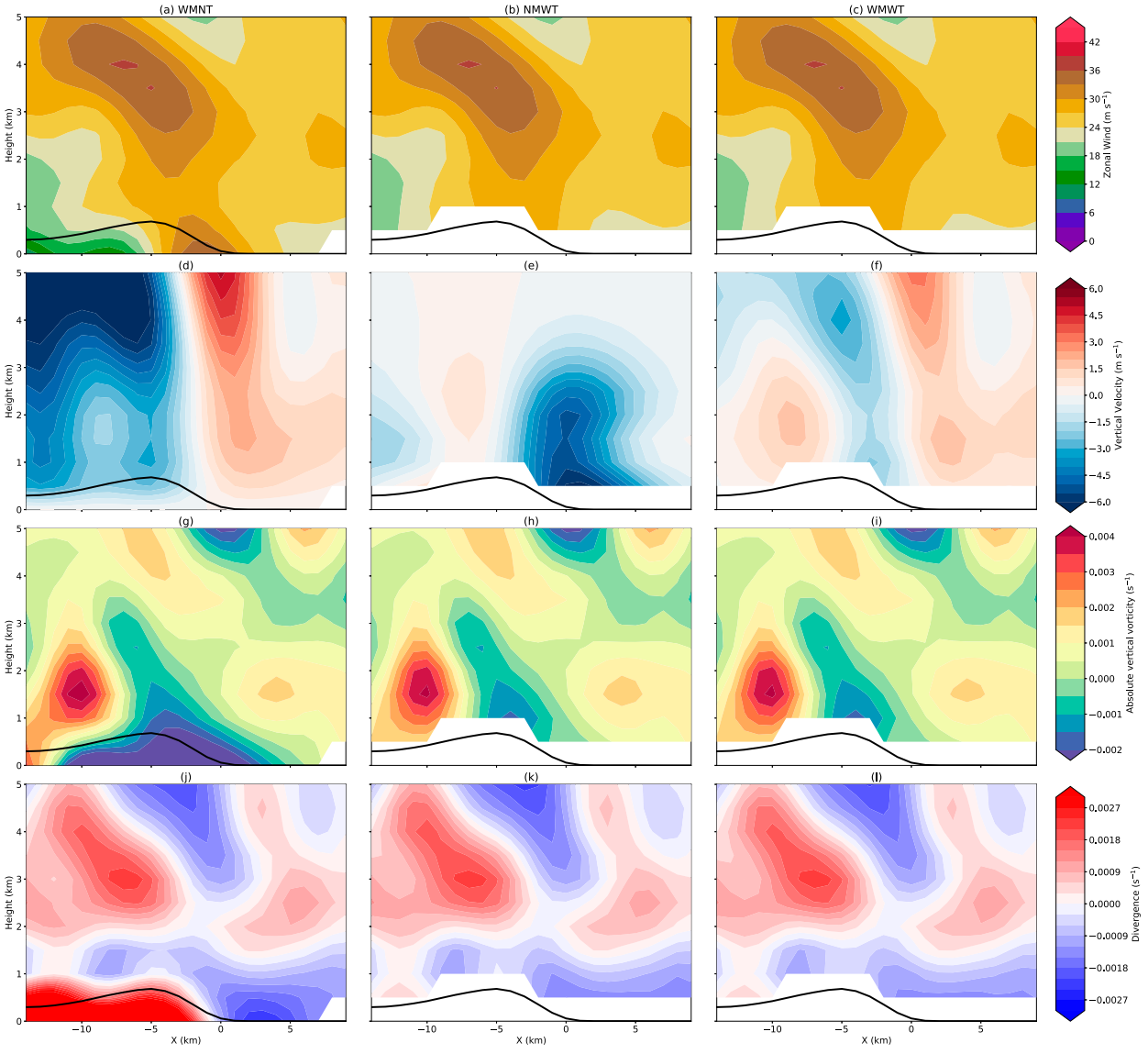

FIG. 13. Same vertical cross section as shown in Fig. 7, but for the (a) WN-NT, (b) NM-WT, and (c) WM-WT experiments, displaying wind speed, vertical velocity, absolute vertical vorticity, and divergence from top to bottom.

6. Summary and discussion

In this study, the immersed boundary method has been successfully implemented into a three-dimensional variational-based multi-Doppler radar wind synthesis algorithm. The performance of the Doppler technique is investigated using model-simulated datasets that are resampled by a radar emulator, providing a more realistic setting for the simulated radar observables. The study explores the sensitivity of various factors

TABLE 4. Configuration of different experimental setups for the grid spacing and Gaussian filter setting. "Grid05" refers to a grid spacing of 0.5 km, and "Filter222" indicates that the Gaussian filter is applied with a setting of 2 in the *i*, *j*, and *k* directions, respectively. For reference, the WRF simulation has a horizontal grid spacing of 1 km.

Name	Grid spacing (km)	Gaussian filter setting (*i*, *j*, *k*)	Approximately resolved scale (km)
Grid05Filter222	0.5	(2, 2, 2)	1
Grid05Filter442	0.5	(4, 4, 2)	2
Grid10Filter222	1.0	(2, 2, 2)	2
Grid10Filter442	1.0	(4, 4, 2)	4

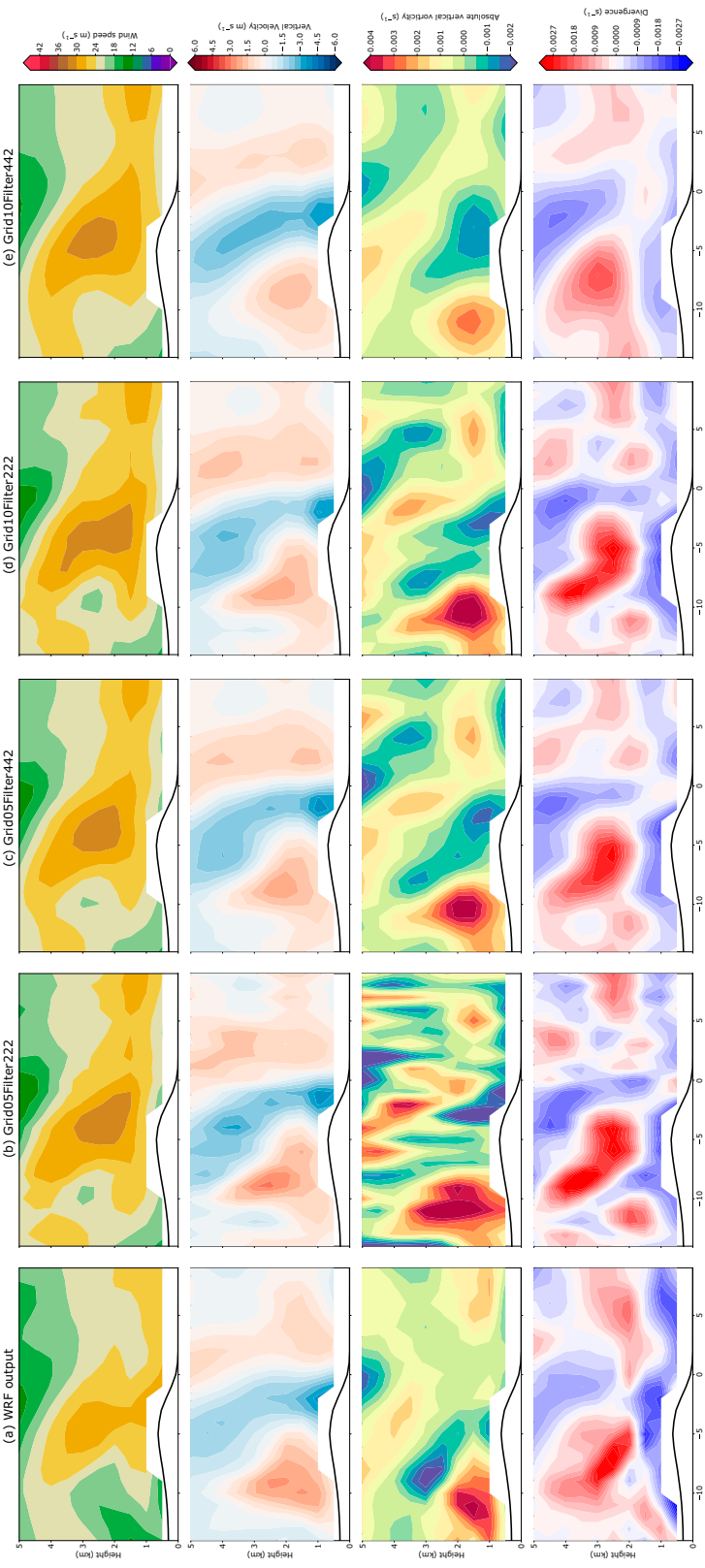

FIG. 14. Same vertical cross section as shown in Fig. 7, but for the following cases: (a) WRF simulation, (b) Grid05Filter222, (c) Grid05Filter442, (d) Grid10Filter222, and (e) Grid10Filter442.

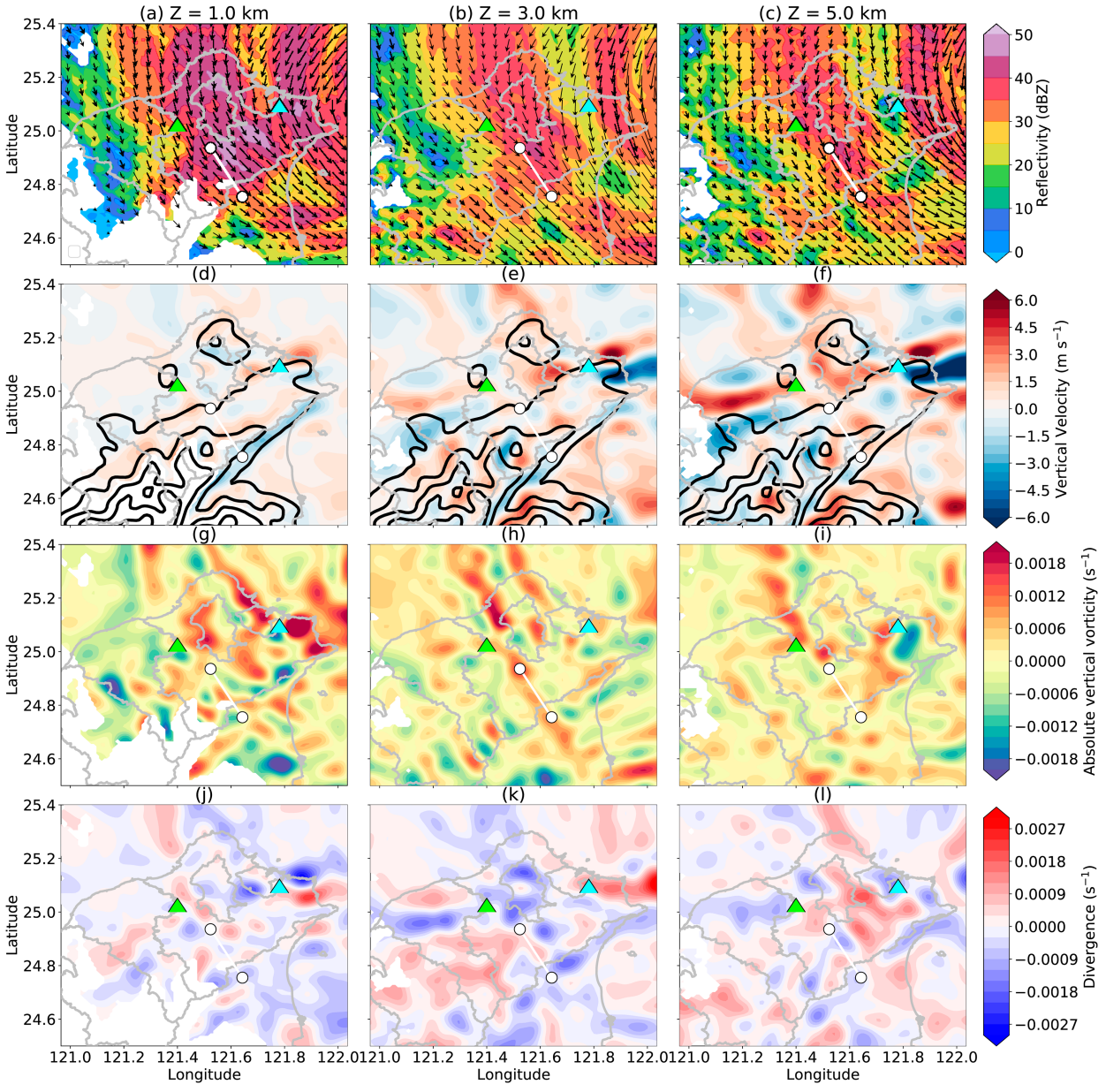

FIG. 15. Horizontal cross sections of (a)–(c) reflectivity, (d)–(f) vertical motion, (g)–(i) absolute vertical vorticity, (j)–(l) divergence at (left) 1-, (center) 3-, and (right) 5-km altitude. The black contour denotes the topography in (d)–(f). The gray contours in the rest of the panels denote the boundaries of the administrative divisions (cities) in Taiwan.

to assess the impact on the accuracy of wind retrieval, including 1) the prescribed strength of Neumann and Dirichlet boundary constraints, 2) the smoothness of complex terrain slope, 3) the algorithm assumptions of mass continuity and terrain boundary, and 4) the grid spacing and Gaussian recursive filter setting. Finally, an observational radar analysis is presented to demonstrate that this new technique can advance scientific analyses in understanding the impact of orographic forcing on precipitation and wind flow using observational datasets.

In this improved SAMURAI technique, the Neumann and Dirichlet boundary conditions are implemented and treated as pseudo-observations, allowing users to adjust the strength of prescribed boundary constraints related to surface impermeability and topographic forcings. Our results from the OSSEs show that the strength of the immersed boundary method constraints can impact the overall retrieval analysis. The sensitivity test shows that the Dirichlet boundary condition generally has a greater impact on the retrieval of vertical wind compared to the Neumann boundary condition. The best analysis is obtained when the boundary constraints are in the same order as the averaged terrain map slope. Additionally, the smoothness of complex terrain slopes is found to

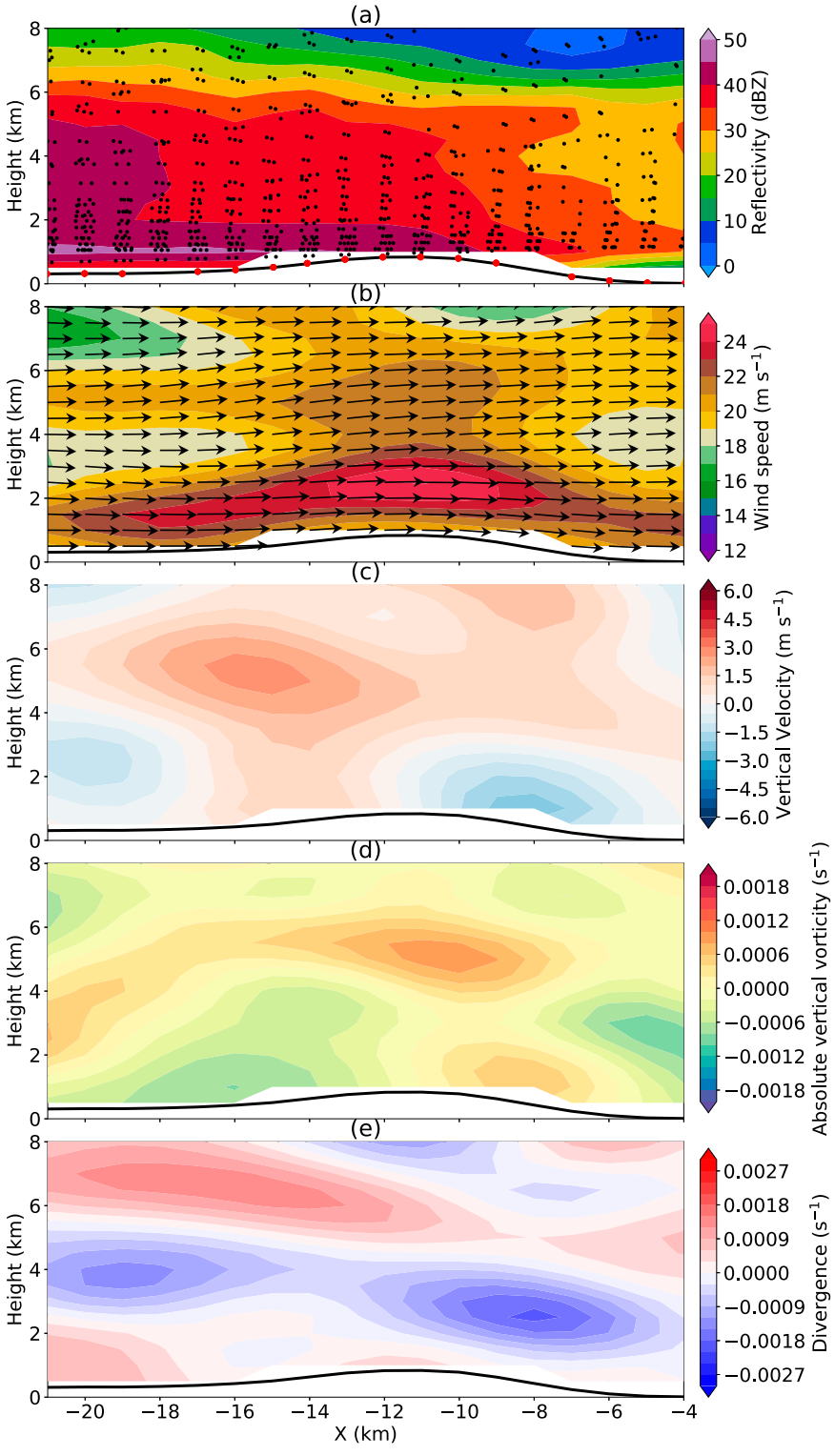

FIG. 16. Vertical cross sections of (a) reflectivity, (b) wind speed, (c) vertical wind, (d) absolute vertical vorticity, and (e) divergence. These cross sections correspond to the white line depicted in Fig. 15. The black dot represents the Doppler radar observations, whereas the red dot represents the pseudo-observations created based on the boundary condition. The black line indicates the topography. The wind vector in (b) illustrates the wind direction and magnitude along the cross section.

influence the overall retrieval. A terrain map with excessively steep slopes for a given grid resolution may produce erroneous results due to the inability to resolve subgrid-scale winds. On the other hand, a terrain map with shallower slopes can provide a relatively smooth retrieval with a better representation of mesoscale features. The algorithm assumptions regarding the mass continuity and the terrain boundary conditions, especially the Dirichlet condition, are essential for generating realistic wind retrieval. Neglecting either of these factors can lead to an incorrect representation of wind retrieval and potential scientific misinterpretation. Considering the terrain boundary conditions within complex terrain areas is necessary to ensure the reliability and validity of the wind retrieval process. The grid spacing and Gaussian recursive filter experiment demonstrate that increasing the Gaussian recursive filter can reduce noise and preserve features with strong signals, but there is a trade-off of losing some detailed structures. In general, it is recommended to use a smaller grid spacing than the data spacing with a larger filter length when data points are sufficient.

Our results are based on a specific dual-Doppler geometry, and therefore, the exact numerical errors may differ in other cases. Caution must be taken when configuring the parameters for optimal analysis retrieval and interpreting the results. In addition, it should be noted that the beam blockage effect resulting from complex terrain was not considered in this study. The beam blockage impact is expected to be minimal based on the domain setup and the specific dual-Doppler geometry used in our analysis, but results may vary in different scenarios or under different terrain and radar configurations. The analysis of both simulated and real radar observations from Typhoon Chanthu (2021) demonstrates that the improved retrieval technique can advance scientific analyses and highlight the potential of using radar observations in advancing our knowledge of orographic precipitation dynamics. Future work will involve conducting additional observational case studies in different regions and weather systems to validate the robustness of the technique and ensure its effectiveness in different scenarios.

Acknowledgments. This research was supported by a Taiwan Ministry of Education graduate fellowship, and the National Science Foundation under Awards AGS-1854559, and SI2-LROSE OAC-1661663 and AGS-2103785. We thank the Central Weather Bureau for providing the ground-based radar data used for this study. We would also like to thank Wen-Chau Lee, Russ S. Schumacher, Kristen L. Rasmussen, Steven C. Reising, and three anonymous reviewers for constructive and helpful comments that improved the paper.

Data availability statement. The dataset used in this research can be found at 10.6084/m9.figshare.21980066. The SAMURAI code can be found at https://github.com/mmbell/samurai.

REFERENCES

Bell, M. M., M. T. Montgomery, and K. A. Emanuel, 2012: Air–sea enthalpy and momentum exchange at major hurricane wind speeds observed during CBLAST. *J. Atmos. Sci.*, **69**, 3197–3222, https://doi.org/10.1175/JAS-D-11-0276.1.

——, M. Dixon, W.-C. Lee, B. Javornik, J. C. DeHart, and T.-Y. Cha, 2021: nsf-lrose/lrose-elle: lrose-elle stable final release 20210312 (lrose-elle-20210312). Zenodo, https://doi.org/10.5281/zenodo.5523312.

Bousquet, O., and M. Chong, 1998: A multiple-Doppler synthesis and continuity adjustment technique (MUSCAT) to recover wind components from Doppler radar measurements. *J. Atmos. Oceanic Technol.*, **15**, 343–359, https://doi.org/10.1175/1520-0426(1998)015<0343:AMDSAC>2.0.CO;2.

Cha, T.-Y., 2023: Investigation of the dynamics of tropical cyclone precipitation structure using radar observations and numerical modeling. Ph.D. thesis, Colorado State University, 125 pp.

——, and M. M. Bell, 2021: Comparison of single-Doppler and multiple-Doppler wind retrievals in Hurricane Matthew (2016). *Atmos. Meas. Tech.*, **14**, 3523–3539, https://doi.org/10.5194/amt-14-3523-2021.

——, ——, W.-C. Lee, and A. J. DesRosiers, 2020: Polygonal eyewall asymmetries during the rapid intensification of Hurricane Michael (2018). *Geophys. Res. Lett.*, **47**, e2020GL087919, https://doi.org/10.1029/2020GL087919.

Chien, F.-C., and H.-C. Kuo, 2011: On the extreme rainfall of Typhoon Morakot (2009). *J. Geophys. Res.*, **116**, D05104, https://doi.org/10.1029/2010JD015092.

Chong, M., and S. Cosma, 2000: A formulation of the continuity equation of MUSCAT for either flat or complex terrain. *J. Atmos. Oceanic Technol.*, **17**, 1556–1565, https://doi.org/10.1175/1520-0426(2000)017<1556:AFOTCE>2.0.CO;2.

——, and Coauthors, 2000: Real-time wind synthesis from Doppler radar observations during the Mesoscale Alpine Programme. *Bull. Amer. Meteor. Soc.*, **81**, 2953–2962, https://doi.org/10.1175/1520-0477(2000)081<2953:RTWSFD>2.3.CO;2.

Colle, B. A., 2004: Sensitivity of orographic precipitation to changing ambient conditions and terrain geometries: An idealized modeling perspective. *J. Atmos. Sci.*, **61**, 588–606, https://doi.org/10.1175/1520-0469(2004)061<0588:SOOPTC>2.0.CO;2.

Collis, S., A. Protat, and K.-S. Chung, 2010: The effect of radial velocity gridding artifacts on variationally retrieved vertical velocities. *J. Atmos. Oceanic Technol.*, **27**, 1239–1246, https://doi.org/10.1175/2010JTECHA1402.1.

Davies-Jones, R. P., 1979: Dual-Doppler radar coverage area as a function of measurement accuracy and spatial resolution. *J. Appl. Meteor.*, **18**, 1229–1233, https://doi.org/10.1175/1520-0450-18.9.1229.

del Moral, A., T. M. Weckwerth, T. Rigo, M. M. Bell, and M. C. Llasat, 2020: C-band dual-Doppler retrievals in complex terrain: Improving the knowledge of severe storm dynamics in Catalonia. *Remote Sens.*, **12**, 2930, https://doi.org/10.3390/rs12182930.

Dennis, J. M., A. H. Baker, B. Dobbins, M. M. Bell, J. Sun, Y. Kim, and T.-Y. Cha, 2022: Enabling efficient execution of a variational data assimilation application. *Int. J. High Perform. Comput. Appl.*, **37**, 101–114, https://doi.org/10.1177/10943420221119801.

Foerster, A. M., M. M. Bell, P. A. Harr, and S. C. Jones, 2014: Observations of the eyewall structure of Typhoon Sinlaku (2008) during the transformation stage of extratropical transition. *Mon. Wea. Rev.*, **142**, 3372–3392, https://doi.org/10.1175/MWR-D-13-00313.1.

Friedrich, K., and M. Hagen, 2004: Evaluation of wind vectors measured by a bistatic Doppler radar network. *J. Atmos.*

Oceanic Technol., **21**, 1840–1854, https://doi.org/10.1175/JTECH-1679.1.

Gamache, J. F., F. D. Marks Jr., and F. Roux, 1995: Comparison of three airborne Doppler sampling techniques with airborne in situ wind observations in Hurricane Gustav (1990). *J. Atmos. Oceanic Technol.*, **12**, 171–181, https://doi.org/10.1175/1520-0426(1995)012<0171:COTADS>2.0.CO;2.

Gao, J., M. Xue, A. Shapiro, and K. K. Droegemeier, 1999: A variational method for the analysis of three-dimensional wind fields from two Doppler radars. *Mon. Wea. Rev.*, **127**, 2128–2142, https://doi.org/10.1175/1520-0493(1999)127<2128:AVMFTA>2.0.CO;2.

——, ——, K. Brewster, and K. K. Droegemeier, 2004: A three-dimensional variational data analysis method with recursive filter for Doppler radars. *J. Atmos. Oceanic Technol.*, **21**, 457–469, https://doi.org/10.1175/1520-0426(2004)021<0457:ATVDAM>2.0.CO;2.

Georgis, J. F., F. Roux, and P. H. Hildebrand, 2000: Observation of precipitating systems over complex orography with meteorological Doppler radars: A feasibility study. *Meteor. Atmos. Phys.*, **72**, 185–202, https://doi.org/10.1007/s007030050015.

Hildebrand, P. H., and C. K. Mueller, 1985: Evaluation of meteorological airborne Doppler radar. Part I: Dual-Doppler analyses of air motions. *J. Atmos. Oceanic Technol.*, **2**, 362–380, https://doi.org/10.1175/1520-0426(1985)002<0362:EOMADR>2.0.CO;2.

——, C. A. Walther, C. L. Frush, J. Testud, and F. Baudin, 1994: The ELDORA/ASTRAIA airborne Doppler weather radar: Goals, design, and first field tests. *Proc. IEEE*, **82**, 1873–1890, https://doi.org/10.1109/5.338076.

——, and Coauthors, 1996: The ELDORA/ASTRAIA airborne Doppler weather radar: High-resolution observations from TOGA COARE. *Bull. Amer. Meteor. Soc.*, **77**, 213–232, https://doi.org/10.1175/1520-0477(1996)077<0213:TEADWR>2.0.CO;2.

Houze, R. A., Jr., 2012: Orographic effects on precipitating clouds. *Rev. Geophys.*, **50**, RG1001, https://doi.org/10.1029/2011RG000365.

Kirshbaum, D. J., and D. R. Durran, 2005: Observations and modeling of banded orographic convection. *J. Atmos. Sci.*, **62**, 1463–1479, https://doi.org/10.1175/JAS3417.1.

Koch, S. E., M. desJardins, and P. J. Kocin, 1983: An interactive Barnes objective map analysis scheme for use with satellite and conventional data. *J. Climate Appl. Meteor.*, **22**, 1487–1503, https://doi.org/10.1175/1520-0450(1983)022<1487:AIBOMA>2.0.CO;2.

Liou, Y.-C., and Y.-J. Chang, 2009: A variational multiple-Doppler radar three-dimensional wind synthesis method and its impacts on thermodynamic retrieval. *Mon. Wea. Rev.*, **137**, 3992–4010, https://doi.org/10.1175/2009MWR2980.1.

——, S.-F. Chang, and J. Sun, 2012: An application of the immersed boundary method for recovering the three-dimensional wind fields over complex terrain using multiple-Doppler radar data. *Mon. Wea. Rev.*, **140**, 1603–1619, https://doi.org/10.1175/MWR-D-11-00151.1.

Lundquist, K. A., F. K. Chow, and J. K. Lundquist, 2010: An immersed boundary method for the Weather Research and Forecasting Model. *Mon. Wea. Rev.*, **138**, 796–817, https://doi.org/10.1175/2009MWR2990.1.

Martinez, J., M. M. Bell, R. F. Rogers, and J. D. Doyle, 2019: Axisymmetric potential vorticity evolution of Hurricane Patricia (2015). *J. Atmos. Sci.*, **76**, 2043–2063, https://doi.org/10.1175/JAS-D-18-0373.1.

Matejka, T., and D. L. Bartels, 1998: The accuracy of vertical air velocities from Doppler radar data. *Mon. Wea. Rev.*, **126**, 92–117, https://doi.org/10.1175/1520-0493(1998)126<0092:TAOVAV>2.0.CO;2.

Morrison, H., J. A. Curry, and V. I. Khvorostyanov, 2005: A new double-moment microphysics parameterization for application in cloud and climate models. Part I: Description. *J. Atmos. Sci.*, **62**, 1665–1677, https://doi.org/10.1175/JAS3446.1.

Nakanishi, M., and H. Niino, 2009: Development of an improved turbulence closure model for the atmospheric boundary layer. *J. Meteor. Soc. Japan*, **87**, 895–912, https://doi.org/10.2151/jmsj.87.895.

North, K. W., M. Oue, P. Kollias, S. E. Giangrande, S. M. Collis, and C. K. Potvin, 2017: Vertical air motion retrievals in deep convective clouds using the ARM scanning radar network in Oklahoma during MC3E. *Atmos. Meas. Tech.*, **10**, 2785–2806, https://doi.org/10.5194/amt-10-2785-2017.

Ooyama, K. V., 1987: Scale-controlled objective analysis. *Mon. Wea. Rev.*, **115**, 2479–2506, https://doi.org/10.1175/1520-0493(1987)115<2479:SCOA>2.0.CO;2.

——, 2002: The cubic-spline transform method: Basic definitions and tests in a 1D single domain. *Mon. Wea. Rev.*, **130**, 2392–2415, https://doi.org/10.1175/1520-0493(2002)130<2392:TCSTMB>2.0.CO;2.

Oue, M., P. Kollias, A. Shapiro, A. Tatarevic, and T. Matsui, 2019: Investigation of observational error sources in multi-Doppler-radar three-dimensional variational vertical air motion retrievals. *Atmos. Meas. Tech.*, **12**, 1999–2018, https://doi.org/10.5194/amt-12-1999-2019.

——, A. Tatarevic, P. Kollias, D. Wang, K. Yu, and A. M. Vogelmann, 2020: The Cloud-Resolving Model Radar Simulator (CR-SIM) version 3.3: Description and applications of a virtual observatory. *Geosci. Model Dev.*, **13**, 1975–1998, https://doi.org/10.5194/gmd-13-1975-2020.

Potvin, C. K., D. Betten, L. J. Wicker, K. L. Elmore, and M. I. Biggerstaff, 2012a: 3DVAR versus traditional dual-Doppler wind retrievals of a simulated supercell thunderstorm. *Mon. Wea. Rev.*, **140**, 3487–3494, https://doi.org/10.1175/MWR-D-12-00063.1.

——, L. J. Wicker, and A. Shapiro, 2012b: Assessing errors in variational dual-Doppler wind syntheses of supercell thunderstorms observed by storm-scale mobile radars. *J. Atmos. Oceanic Technol.*, **29**, 1009–1025, https://doi.org/10.1175/JTECH-D-11-00177.1.

Protat, A., and I. Zawadzki, 1999: A variational method for real-time retrieval of three-dimensional wind field from multiple-Doppler bistatic radar network data. *J. Atmos. Oceanic Technol.*, **16**, 432–449, https://doi.org/10.1175/1520-0426(1999)016<0432:AVMFRT>2.0.CO;2.

Purser, R. J., W.-S. Wu, D. F. Parrish, and N. M. Roberts, 2003: Numerical aspects of the application of recursive filters to variational statistical analysis. Part I: Spatially homogeneous and isotropic Gaussian covariances. *Mon. Wea. Rev.*, **131**, 1524–1535, https://doi.org/10.1175//1520-0493(2003)131<1524:NAOTAO>2.0.CO;2.

Ray, P. S., J. J. Stephens, and K. W. Johnson, 1979: Multiple-Doppler radar network design. *J. Appl. Meteor.*, **18**, 706–710, https://doi.org/10.1175/1520-0450(1979)018<0706:MDRND>2.0.CO;2.

——, C. L. Ziegler, W. Bumgarner, and R. J. Serafin, 1980: Single- and multiple-Doppler radar observations of tornadic storms. *Mon. Wea. Rev.*, **108**, 1607–1625, https://doi.org/10.1175/1520-0493(1980)108<1607:SAMDRO>2.0.CO;2.

Singh, J., and Coauthors, 2021: Effects of spatial resolution on WRF v3.8.1 simulated meteorology over the central Himalaya. *Geosci. Model Dev.*, **14**, 1427–1443, https://doi.org/10.5194/gmd-14-1427-2021.

Skamarock, W. C., and Coauthors, 2021: A description of the Advanced Research WRF Model version 4.3. NCAR Tech. Note NCAR/TN-556+STR, 165 pp., https://doi.org/10.5065/1dfh-6p97.

Smith, R. B., and I. Barstad, 2004: A linear theory of orographic precipitation. *J. Atmos. Sci.*, **61**, 1377–1391, https://doi.org/10.1175/1520-0469(2004)061<1377:ALTOOP>2.0.CO;2.

Steiner, M., 1991: A new relationship between mean Doppler velocity and differential reflectivity. *J. Atmos. Oceanic Technol.*, **8**, 430–443, https://doi.org/10.1175/1520-0426(1991)008<0430:ANRBMD>2.0.CO;2.

Tseng, Y.-H., and J. H. Ferziger, 2003: A ghost-cell immersed boundary method for flow in complex geometry. *J. Comput. Phys.*, **192**, 593–623, https://doi.org/10.1016/j.jcp.2003.07.024.

U.S./Japan ASTER Science Team, 2019: ASTER global digital elevation model V003. NASA EOSDIS Land Processes DAAC, accessed 24 October 2022, https://doi.org/10.5067/ASTER/ASTGTM.003.

Zipser, E. J., D. J. Cecil, C. Liu, S. W. Nesbitt, and D. P. Yorty, 2006: Where are the most intense thunderstorms on Earth? *Bull. Amer. Meteor. Soc.*, **87**, 1057–1072, https://doi.org/10.1175/BAMS-87-8-1057.